

Strain-Tuned Incommensurate Kekulé Spiral Order in Twisted Bilayer Graphene: a Quantum Many-Body Study

Cheng Huang,^{1,2,*} Yves H. Kwan,^{3,4,*} Maksim Ulybyshev,⁵ Fakher F. Assaad ,^{5,6} Laura Classen,^{7,8} and Zi Yang Meng^{1,2}

¹*Department of Physics and HK Institute of Quantum Science & Technology,
The University of Hong Kong, Pokfulam Road, Hong Kong SAR, China*

²*State Key Laboratory of Optical Quantum Materials,
The University of Hong Kong, Pokfulam Road, Hong Kong SAR, China*

³*Department of Physics, University of Texas at Dallas, Richardson, Texas 75080, USA*

⁴*Princeton Center for Theoretical Science, Princeton University, Princeton, NJ 08544*

⁵*Institut für Theoretische Physik und Astrophysik, Universität Würzburg, 97074 Würzburg, Germany*

⁶*Würzburg-Dresden Cluster of Excellence ctd.qmat, Am Hubland, 97074 Würzburg, Germany*

⁷*Max Planck Institute for Solid State Research, Heisenbergstr. 1, 70569 Stuttgart Germany*

⁸*School of Natural Sciences, Technische Universität München, 85748 Garching, Germany*

(Dated: May 21, 2026)

The understanding of quantum many-body states in twisted bilayer graphene at the magic angle has been greatly improved both in experiment and in theory. However, away from the exactly solvable chiral limit and the sign-problem-free charge neutrality point, the calculation of the ground state properties and the identification of the phase diagram are challenging due to the exponential increase in the complexity, which has rendered explanations of experimentally observed insulating and superconducting phases restricted largely to the perturbative level. Here we focus on the filling factors $\nu = \pm 2$ away from charge neutrality and address the question of the strain dependence of the interacting ground state. We adjust our continuous field momentum-space quantum Monte Carlo (QMC) method to treat the sign problem approximately, and perform a quantum many-body study together with exact diagonalization (ED) and Hartree-Fock (HF) mean field. Leveraging this combined protocol of QMC, ED, and HF, we investigate the strain-tuned transition from the Kramers intervalley coherent (KIVC) state to the incommensurate Kekulé spiral state (IKS). Our computational protocol sheds light on the KIVC-IKS transition in a projected correlated flat-band setting, and opens the door for further understanding of the rich phase diagram of twisted bilayer graphene and other strongly-correlated flat-band systems.

I. INTRODUCTION

Understanding the phase diagram of twisted bilayer graphene (TBG) has remained an enduring pursuit in strongly-correlated moiré materials since the observation of superconductivity and correlated insulating behavior at the magic angle $\theta \approx 1.05^\circ$ [1, 2]. Beyond the twist angle, it has been recognized that strain considerably alters the physics of realistic TBG devices. In particular, uniaxial heterostrain, which is often present with strength $\epsilon_s \sim 0.1\% - 0.7\%$ [3–7], breaks C_3 rotation symmetry and significantly enhances the non-interacting bandwidth of the central moiré bands [8, 9]. At charge neutrality, strain has been argued to drive a transition from a correlated insulator to a semimetal [10], the latter being consistent with most experiments. Furthermore, the incommensurate Kekulé spiral (IKS) state has been experimentally identified using scanning tunneling microscopy as the ground state for typical devices of TBG with heterostrain at filling factors near $\nu = \pm 2$ [11, 12], after predictions from Hartree-Fock mean field calculations of a gapped IKS at $\nu = \pm 2, \pm 3$ [13, 14].

The IKS involves intervalley coherence (IVC) between the microscopic graphene valleys, thereby breaking $U_\nu(1)$ -valley symmetry. While various candidate strong-coupling insulators in the unstrained limit, such as the so-called Kramers intervalley coherent (KIVC) state [15, 16], also exhibit IVC, the IKS is unique in that the valleys only hybridize with an

incommensurate moiré spiral wavevector \mathbf{q}_{IKS} . This further breaks the moiré translation symmetry [13].

The IKS also differs from the well-studied strong-coupling insulators in other important ways. The strong-coupling states closely resemble simple quantum Hall ferromagnets, and are rooted in an emergent $U(4) \times U(4)$ -symmetric limit of TBG which accommodates exact Slater determinantal ground states [15–19]. On the other hand, the IKS is stabilized in the ‘intermediate-coupling’ regime where interactions and kinetic dispersion compete on a similar footing, which has so far precluded exactly solvable limits and complicated analytical approaches [20, 21]. At a mean-field level, it has also been shown that the Euler topology of the central bands [22, 23], which is protected by combined C_2 and spinless time-reversal symmetry \mathcal{T} , imposes a complex momentum-space texture of the IVC in the IKS [14, 24]. However, it is not clear how the phase diagram and topological constraints of the IKS behave beyond the approximations of mean-field theory.

The above experimental and theoretical considerations motivate quantum many-body numerical calculations of the phase diagram of strained TBG and the IKS. While a previous density matrix renormalization group (DMRG) study has investigated the competition between the IKS and other phases at $\nu = -3$ [25], here we perform continuous field momentum-space quantum Monte Carlo (QMC) [26, 27] simulations at $\nu = -2$, where we also anticipate fewer complications from non-trivial spin physics. (Due to the approximate particle-hole symmetry of our Hamiltonian, the physics at $\nu = +2$ will be similar.) In the absence of strain, the QMC simulation at the

* These authors contributed equally to this work.

charge neutrality point ($\nu = 0$) is sign-problem-free thanks to an anti-unitary symmetry [27, 28]. At the other integer fillings close to the chiral limit where the ground state is a gapped insulator, the sign-problem is only polynomial due to the sign bound [29, 30] such that one can still push to large system sizes [31].

In the present modelling of realistic and strained TBG, the anti-unitary symmetry and the sign bound are violated, leading to the conventional exponential sign problem [32]. We make an approximation by taking the absolute value of the original sampling weight as the new sampling weight. We show that such an approximation preserves moiré translation, $C_2\mathcal{T}$, and valley- $U(1)$ symmetries, which are relevant symmetries for the many-body phases we are interested in. We further justify our treatment of the sampling weight by benchmarking with exact diagonalization (ED) on small systems to confirm that these two approaches yield similar electron occupation distributions and intervalley structure factors. For larger system sizes, our approximated QMC simulation yields results for the electron occupation distribution and IKS nesting diagnostics that are consistent with Hartree-Fock (HF) numerics.

This comparison sheds light on the ‘intermediate-coupling’ nature of the IKS in the strained regime, and illustrates how the moiré spiral wavevector \mathbf{q}_{IKS} can be captured by the approximated QMC, at least at the level of one-body diagnostics. Our combined protocol of QMC, ED, and HF therefore probes the essence of the strain-induced correlated ground state at the semi-quantitative level, and paves the way for more accurate quantum many-body treatments of this challenging problem. We also investigate the strain-tuned transition from the KIVC at small strains to IKS at large strains, and discuss the Euler topology of the central bands and its impact on the occupation number distribution. We believe our methodology and results enhance the foundation for understanding the many-body ground states of magic-angle TBG in realistic settings.

II. RESULTS

Model and QMC+ED+HF computational protocol. — Our calculations are performed on the interacting Bistritzer-MacDonald (BM) model [33], which we briefly outline below (more details are provided in Methods). The non-interacting (kinetic) BM Hamiltonian acts on a basis of plane waves with creation operator $c_{s,\eta,l,\sigma}^\dagger(\mathbf{k})$, where \mathbf{k} is the plane wave momentum, $s = \uparrow, \downarrow$ is the spin, $\eta = \pm$ is the valley, $l = 1, 2$ is the layer, and $\sigma = A, B$ is the sublattice.

In the absence of strain, there are two kinetic contributions. The first consists of rotated Dirac cones from each layer with Dirac velocity $\frac{\hbar v_{\text{F}}}{\sqrt{3}a} = 2.37745$ eV, where $a = 1.42$ Å is the nearest neighbor carbon distance. The second contribution captures the interlayer moiré hopping, and is parameterized by intra-sublattice and inter-sublattice tunneling constants u_0 and u_1 . Note that u_0/u_1 is expected to lie in the range of $\sim 0.5 - 0.8$ due to lattice relaxation, corrugation, and renormalization effects [34–37]. We set $u_0 = 80$ meV, $u_1 = 110$ meV, and the twist angle $\theta = 1.15^\circ$.

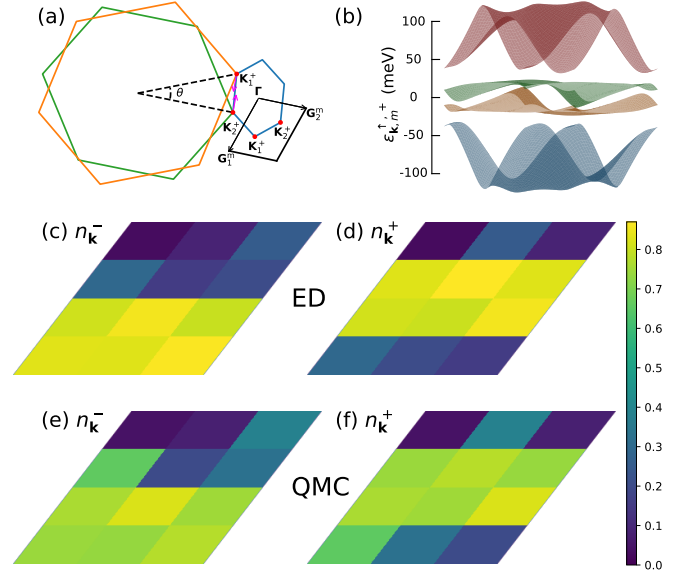


Fig. 1. Strained Brillouin zones, shifted Dirac points, and occupation number comparison between ED and approximated QMC. (a) Schematic Brillouin zones (green and orange hexagons) of two graphene layers with interlayer twist θ and uniaxial heterostrain of $\pm\epsilon_s/2$ for each layer. The corresponding strained moiré Brillouin zone (mBZ) in the $\eta = +$ valley can be represented by the blue hexagon or black rhombus, with Γ the mBZ center, $\mathbf{G}_{1,2}^m$ the moiré reciprocal lattice vectors, and $\mathbf{K}_{1,2}^+$ the mBZ corners. The magenta arrows show the exaggerated deviations of the monolayer Dirac cones. (b) The low-energy moiré bands with strain $\epsilon_s = 0.6\%$ for valley $\eta = +$ and spin $s = \uparrow$. See Fig. S1 for the deviations of the deformed Dirac cones from the mBZ corners with various strains. (c,d) and (e,f) show $n^\eta(\mathbf{k})$ from ED and approximated QMC respectively for the system size of 4×3 and $\epsilon_s = 0.6\%$. We consider a spinless calculation, so that $\nu = -1$ here (the remote valence gap corresponds to $\nu = -2$).

In graphene, uniaxial strain with strength ϵ_s and orientation ϕ_s is characterized by the tensor

$$S(\epsilon_s, \phi_s) = \begin{pmatrix} \cos \phi_s & \sin \phi_s \\ -\sin \phi_s & \cos \phi_s \end{pmatrix} \begin{pmatrix} -\epsilon_s & 0 \\ 0 & \nu_s \epsilon_s \end{pmatrix} \begin{pmatrix} \cos \phi_s & -\sin \phi_s \\ \sin \phi_s & \cos \phi_s \end{pmatrix}, \quad (1)$$

with Poisson ratio $\nu_s = 0.16$. For a bilayer system, uniaxial heterostrain of magnitude ϵ_s corresponds to layer-dependent $\epsilon_{s,1} = -\epsilon_{s,2} = -\frac{\epsilon_s}{2}$ and $\phi_{s,1} = \phi_{s,2} = \phi_s$. As illustrated in Fig. 1(a), it not only deforms the moiré reciprocal lattice vectors (RLVs) \mathbf{G} , but also shifts the positions of the monolayer Dirac cones, both in momentum and energy [38] (see Methods and SI Fig. S1). We set the strain direction from the horizontal as $\phi_s = 130^\circ$ counter-clockwise.

The strained BM model can be rewritten as

$$H_0 = \sum_{s,\eta,\mathbf{k},m} \left(\epsilon_{\mathbf{k},m}^{s,\eta} - \mu \right) c_{s,\eta,\mathbf{k},m}^\dagger c_{s,\eta,\mathbf{k},m} \quad (2)$$

using the BM basis

$$c_{s,\eta,\mathbf{k},m}^\dagger = \sum_{\mathbf{G},l,\sigma} U_{\mathbf{k},m,\mathbf{G},l,\sigma}^{s,\eta} c_{s,\eta,l,\sigma}^\dagger(\mathbf{k} + \mathbf{G}), \quad (3)$$

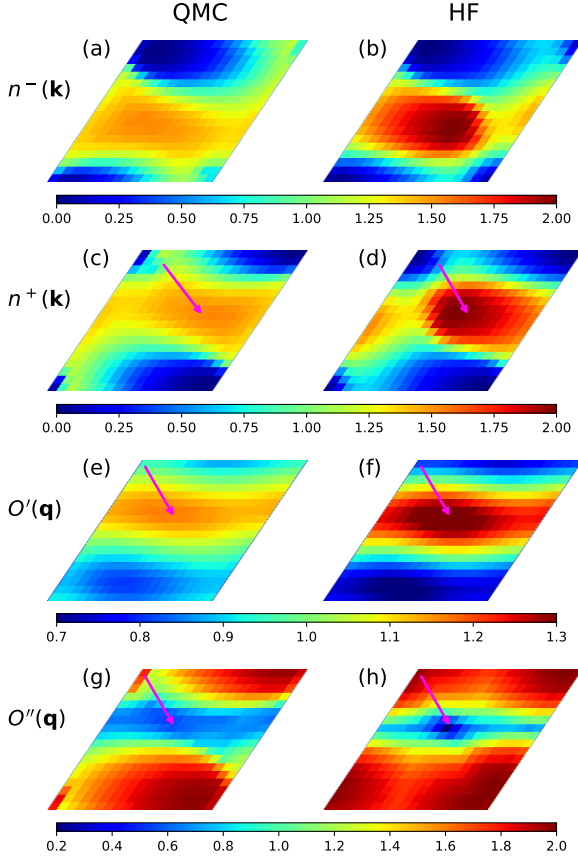


Fig. 2. **Occupation number $n^\eta(\mathbf{k})$ and corresponding nesting diagnostics from QMC and HF at $\nu = -2$ with $N_{\mathbf{k}} = 18 \times 18$ and strain strength $\epsilon_s = 0.6\%$.** The left panels are the QMC data, where (a) and (c) show the occupation factor $n^\eta(\mathbf{k})$. The magenta arrow in (c) points from the minimum in (a) to the maximum in (c). The magenta arrow in (e) [(g)] corresponds to the maximum [minimum] of $O'(\mathbf{q})$ [$O''(\mathbf{q})$]. The right panels are the corresponding data for the HF ground state which has IKS wavevector $\mathbf{q}_{\text{IKS}} = (7/18, 7/18)$.

where m is the band index, and \mathbf{k} is a moiré momentum within the mBZ. In our numerical calculations, the mBZ is discretized into a momentum grid with $N_{\mathbf{k}} = L_1 \times L_2$ points, corresponding to the number of moiré unit cells. Strain significantly affects the moiré band structure $\epsilon_{\mathbf{k},m}^{s,\eta}$ and corresponding Bloch eigenvectors $U_{\mathbf{k},m,G,l,\sigma}^{s,\eta}$. The dispersion $\epsilon_{\mathbf{k},m}^{s,\eta}$ is plotted for $\epsilon_s = 0.6\%$, $s = \uparrow$, and $\eta = +$ in Fig. 1 (b). The evolution of the two low-energy bands with strain strength ϵ_s is shown in Fig. S1 in SI [39]. For $\epsilon_s < 0.6\%$, the indirect gap between the central and remote bands is still $\gtrsim 20$ meV (Fig. 1 (b)), which is larger than the typical interaction scale [26]. Therefore in this work, we project to the central two bands per spin and valley, which should qualitatively capture the relevant physics. The chemical potential μ is introduced to control the moiré filling factor ν in QMC.

Long-range density-density interactions are incorporated as

$$H_I = \sum_{\mathbf{Q}>0} \frac{1}{4\Omega} V(\mathbf{Q}) (A_{\mathbf{Q}}^2 - B_{\mathbf{Q}}^2) \quad (4)$$

where $A_{\mathbf{Q}} = \delta\rho_{-\mathbf{Q}} + \delta\rho_{\mathbf{Q}}$, $B_{\mathbf{Q}} = \delta\rho_{-\mathbf{Q}} - \delta\rho_{\mathbf{Q}}$, Ω is the total real-space system area, and the summation over momentum transfers $\mathbf{Q} > 0$ runs over half of momentum space (i.e. only one of \mathbf{Q} or $-\mathbf{Q}$ is included) and excludes $\mathbf{Q} = 0$ (see Methods). The density operator (See Methods for the derivation of Eq. (5)) is

$$\delta\rho_{\mathbf{Q}} = \sum_{s,\eta,k,m,n} \lambda_{m,n}^{s,\eta}(\mathbf{k}, \mathbf{Q}) \times \left(c_{s,\eta,\mathbf{k},m}^\dagger c_{s,\eta,\mathbf{k}+\mathbf{Q},n} - \frac{1}{2} \delta_{\mathbf{Q} \in \text{RLV}} \delta_{m,n} \right). \quad (5)$$

The form factor

$$\lambda_{m,n}^{s,\eta}(\mathbf{k}, \mathbf{Q}) = \sum_{G,l,\sigma} [U_{\mathbf{k},m,G,l,\sigma}^{s,\eta}]^* U_{\mathbf{k}+\mathbf{Q},n,G,l,\sigma}^{s,\eta} \quad (6)$$

arises from rotation from the plane-wave basis to the band basis. Since we have projected to the central bands, the $\frac{1}{2}$ term in Eq. (5) corresponds to the ‘central average’ interaction scheme utilized in e.g. Refs. [15, 16], which preserves the approximate many-body particle-hole symmetry. We note that this form of Eq. (5) is slightly different from that used in some previous QMC works where $\delta\rho_{\mathbf{Q}}$ depends on filling factor and the sign problem at integer filling is only polynomial [29, 30].

We use the single-gate-screened Coulomb potential $V(\mathbf{Q}) = \frac{e^2}{2\epsilon_0\epsilon_r|\mathbf{Q}|} (1 - e^{-|\mathbf{Q}|d})$, with a screening parameter $d = 20$ nm and dielectric constant $\epsilon_r = 10$. In the summation over momentum transfers \mathbf{Q} in Eq. (4), we impose a circular cutoff whose radius is the length of the longest primitive moiré RLV. This is a reasonable approximation due to the decay of the Coulomb potential and form factors [26].

We tackle the total Hamiltonian $H = H_0 + H_I$ using ED, approximated QMC and self-consistent HF techniques. For the QMC, we apply the continuous field momentum-space method with Hamiltonian dynamics [26] to simulate H for temperature $T = 0.167$ meV at $L_1 = L_2 = 18$.

To explain our approximated QMC treatment, we start with a general operator \hat{O} that is measured as

$$\langle \hat{O} \rangle = \frac{\int dC O_C W_C}{\int dC W_C} = \frac{\int dC O_C \frac{W_C}{\text{Re}(W_C)} \text{Re}(W_C)}{\int dC \text{Re}(W_C)} \quad (7)$$

where C is a configuration of auxiliary fields, O_C is the value of \hat{O} in C , the sampling weight W_C is generally complex, and the reality of the partition function leads to $\int dC W_C = \int dC \text{Re}(W_C)$. (See Methods for the explicit expression for W_C). Therefore, performing importance sampling over the auxiliary field with the sampling weight $\text{Re}(W_C)$ yields the expectation value $\langle \hat{O} \rangle$.

Away from the charge neutrality point ($\nu = 0$), the sampling weight $\text{Re}(W_C)$ can become negative [26, 27, 30, 31], which introduces significant difficulty in obtaining reliable statistics. To ameliorate this problem, we make an approximation by replacing the true sampling weight in Eq. (7) by its absolute magnitude $|\text{Re}(W_C)|$ which corresponds to a modified statistical ensemble. In other words, we evaluate $\langle \hat{O} \rangle$ according

to

$$\langle \hat{O} \rangle \leftarrow \frac{\int dCO_C \frac{W_C}{\text{Re}(W_C)} |\text{Re}(W_C)|}{\int dC |\text{Re}(W_C)|}. \quad (8)$$

While this procedure is certainly an approximation, its application to our particular context of TBG merits additional comment. In the SI [39], we prove that the approximated treatment shares the same symmetries as the original Hamiltonian, and therefore does not introduce explicit breakings in the important symmetries that we wish to investigate. While the density matrix remains Hermitian, it may lack positive definiteness in this approximation. This implies complex eigenvalues of the effective Hamiltonian with imaginary part quantized to $m\pi/\beta$, m being an integer. At high temperatures where the sign problem is not severe, we can expect $m = 0$. At lower temperatures, we have to test this numerically by e.g. explicitly computing the density matrix for small subsystems or by analyzing time displaced correlation function to assess if the density matrix remains positive definite (see discussion SI Sec. S5 [39]).

Overall, we do not make any claim regarding the general applicability of our approach for tackling the sign problem in QMC simulations. Rather, we propose that for the specific and challenging problem of the strain-induced correlated ground state of TBG at filling $\nu = \pm 2$, our approach, combining approximated QMC with ED and HF, provides a promising pathway to understand the quantum many-body ground state.

Results on density distribution. — To demonstrate the qualitative correctness of our approximated QMC approach, we first benchmark against ED on a spinless system of size 4×3 by comparing the occupation numbers (note that the spin index s below is neglected for a spinless calculation)

$$n^\eta(\mathbf{k}) = \left\langle \sum_{s,m} c_{s,\eta,\mathbf{k},m}^\dagger c_{s,\eta,\mathbf{k},m} \right\rangle. \quad (9)$$

Figs. 1 (c)-(f) show $n^\eta(\mathbf{k})$ computed at $\epsilon_s = 0.6\%$ from ED and QMC on the 4×3 mBZ grid. The electron occupation numbers are quantitatively consistent, with only minor differences of the order of ~ 0.1 (for a quantity that can vary between 0 and 2 for a spinless calculation, according to the definition) for some momenta. Importantly, both calculations exhibit a similar inhomogeneous distribution of the electron occupation across the mBZ, with a pronounced minimum at Γ_M ($\mathbf{k} = 0$). As we discuss later, the momentum-space modulation of $n^\eta(\mathbf{k})$ will influence the selection of the IKS wavevector \mathbf{q}_{IKS} when we examine larger sizes such as 18×18 . We note for the ED calculation, the 4×3 calculation contains 48 single-particle orbitals (12 mBZ momenta with 2 bands and 2 valleys). The largest symmetry sector has a Hilbert space dimension of $\sim 1.6 \times 10^9$, which is of the same order or larger than those considered in previous ED studies in TBG [40, 41].

In SI Fig. S5 and Fig. S6, we also provide a comparison of both $n^\eta(\mathbf{k})$ and the intervalley structure factors (see the definition in Eq. 14) for the 2×2 and 3×3 systems, where we are further able to perform the non-approximated QMC (i.e. using Eq. (7) with the exponential sign problem). Not only do the occupation numbers $n^\eta(\mathbf{k})$ match well across non-

approximated QMC, approximated QMC and ED, but we also find that the KIVC structure factors $S_{\text{KIVC}}(\mathbf{q})$ are consistent.

For the self-consistent HF calculations of H , we follow the standard numerical procedure described in e.g. Refs. [13, 42]. The HF framework involves searching for the lowest-energy state in the manifold of single Slater determinants. As we are interested in the IKS, we constrain the Slater determinants to preserve a modified translation symmetry with intervalley spiral moiré wavevector \mathbf{q} . At the level of the one-body density matrix, this corresponds to the parameterization

$$\langle c_{s,\eta,\mathbf{k},m}^\dagger c_{s',\eta,\mathbf{k}',n} \rangle = \delta_{s,s'} \delta_{\mathbf{k},\mathbf{k}'} P_{\eta,m;\eta,n}(\mathbf{k}, s), \quad (10)$$

$$\langle c_{s,-,\mathbf{k},m}^\dagger c_{s',+,\mathbf{k}',n} \rangle = \delta_{s,s'} \delta_{\mathbf{k}+\mathbf{q},\mathbf{k}'} P_{-,m;+,n}(\mathbf{k}, s). \quad (11)$$

Note that intervalley coherence in the HF state is only permitted between \mathbf{k} in valley $\eta = -$ and $\mathbf{k} + \mathbf{q}$ in valley $\eta = +$. If the HF solution corresponds to an IKS, we further enforce it to satisfy $SU(2)_S$ spin-rotation invariance, as this has been shown to capture the lowest energy state in our present modelling of the TBG Hamiltonian [43]. For an IKS state, we also refer to the intervalley wavevector \mathbf{q} as the IKS wavevector \mathbf{q}_{IKS} . The HF ground state is obtained by performing HF calculations with multiple initial seeds for all \mathbf{q} in the mBZ and minimizing over the total energies. We note that the ordering wavevector is very soft, in the sense that IKS states with considerably different values of \mathbf{q}_{IKS} can have closely competing energy differences of $\lesssim 1$ meV per unit cell [13] (see also Fig. S3 in SI [39]).

Diagnostics for IKS. — In Figs. 2 (a) - (d) and Fig. 3 (a) - (d), we first compare the occupation numbers obtained in QMC and HF at $\nu = -2$ for $\epsilon_s = 0.6\%$ and 0.3% respectively. The HF ground state corresponds to an IKS for both strains, albeit with different \mathbf{q}_{IKS} , and TRS in the IKS leads to $n^+(\mathbf{k}) = n^-(-\mathbf{k})$. The approximated QMC does not find long-range IKS order, as discussed further below. Interestingly, we find qualitative agreement in $n^\eta(\mathbf{k})$ using the two numerical techniques. The occupation number distribution is highly inhomogeneous across the mBZ. For instance, there is a strong depletion of electron population around Γ_M , while there is a ‘lobe’ of high electron occupation at a non-zero \mathbf{k} . The position of this high-occupation lobe is similar in the QMC and HF calculations. We note that in the HF framework, $n^\eta(\mathbf{k})$ would be integer-valued in the absence of IVC. Hence, the fact that $n^\eta(\mathbf{k})$ evolves continuously with \mathbf{k} in panels (a) - (d) can be traced directly to the presence of IVC.

To connect the above observations to IKS physics, we first note that a mean-field IKS exactly satisfies $n^+(\mathbf{k} + \mathbf{q}_{\text{IKS}}) + n^-(\mathbf{k}) = \bar{n}$, where $\bar{n} = 2$ is the average occupation factor (including both spins and valleys) over the mBZ. It has further been theoretically shown that $n^\eta(\mathbf{k})$ of the IKS, which preserves C_2 and \mathcal{T} symmetry, cannot be homogeneous over the mBZ, at least at mean-field level [24, 44]. This arises from the non-trivial $C_2\mathcal{T}$ -protected Euler index of the pair of central bands within each spin-valley flavor [22, 23], which topologically mandates them to be connected by Dirac points. Any single $C_2\mathcal{T}$ -symmetric band constructed from this pair is hence necessarily singular. In the projected model, the insulating IKS at $\nu = -2$ however contains only a single occupied IVC band within each spin sector. This forces $n^\eta(\mathbf{k})$ to take the

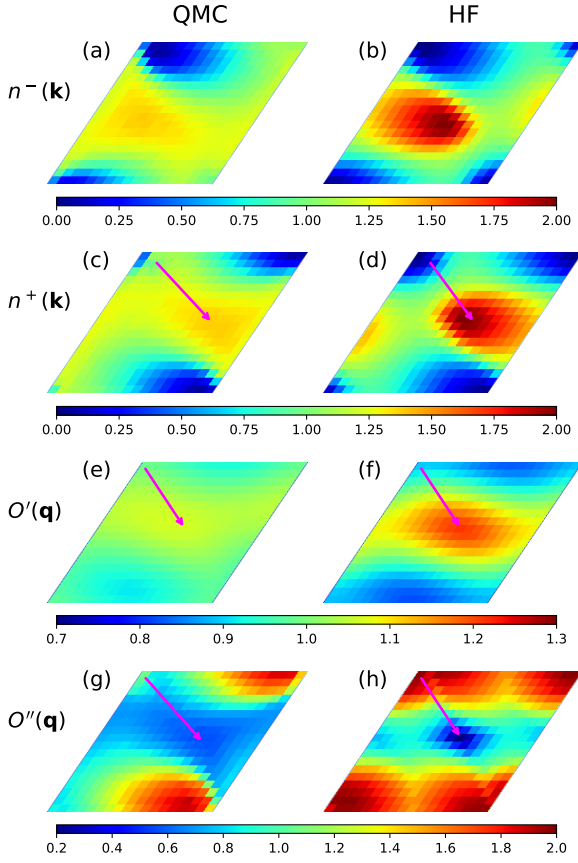


Fig. 3. Occupation number n^η and corresponding nesting diagnostics from QMC and HF at $\nu = -2$ with $N_{\mathbf{k}} = 18 \times 18$ and strain strength $\epsilon_s = 0.3\%$. The left panels are the QMC data, where (a) and (c) show the occupation factor $n^\eta(\mathbf{k})$. The magenta arrow in (c) points from the minimum in (a) to the maximum in (c). The magenta arrow in (e) [(g)] corresponds to the maximum [minimum] of $O'(\mathbf{q})$ [$O''(\mathbf{q})$]. The right panels are the corresponding data for the HF ground state which has IKS wavevector $\mathbf{q}_{\text{IKS}} = (8/18, 9/18)$.

minimal ($n^\eta(\mathbf{k}) = 0$) and maximal values ($n^\eta(\mathbf{k}) = 2$) somewhere in the mBZ [24] in order to ‘hide’ these singularities and form a well-behaved insulator. Therefore, unlike a strong-coupling IVC state such as the KIVC, the valley-resolved occupation factor of a mean-field IKS is topologically required to modulate significantly across the mBZ.

The above considerations enable a first estimation of the wavevector \mathbf{q}_{IKS} if an IKS state is indeed present. The idea is to match the location $\mathbf{k}_{\text{min}}^-$ of the occupation factor minimum in valley $\eta = -$ to the location $\mathbf{k}_{\text{max}}^+$ of the maximum in valley $\eta = +$. In the mean-field IKS, these momenta will hybridize with each other to satisfy $n^+(\mathbf{k} + \mathbf{q}_{\text{IKS}}) + n^-(\mathbf{k}) = \bar{n}$. From this, we therefore extract $\mathbf{q}_{\text{IKS}} = \mathbf{k}_{\text{max}}^+ - \mathbf{k}_{\text{min}}^-$, which is plotted as the magenta arrows in panels (c) and (d). In the QMC, we find that the value of \mathbf{q}_{IKS} extracted this way is similar to the HF result for the two strains considered, and differs by only one momentum spacing on the 18×18 mesh. In Fig. 2 (a) - (d) and Fig. 3 (a) - (d), the fact that the electron depletion region ($n^\eta(\mathbf{k}) \simeq 0$) occurs near $\mathbf{k}_{\text{min}}^\eta \simeq \Gamma_{\text{M}}$ can be rationalized from the combination of strain, which pushes the non-interacting

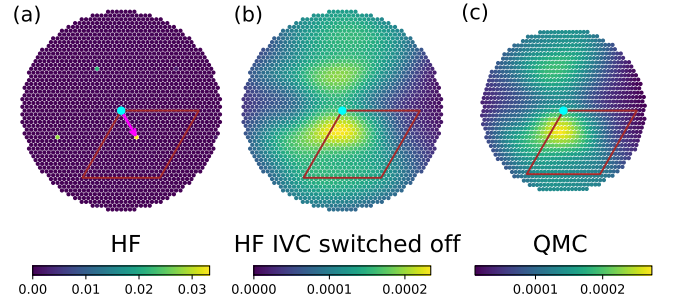


Fig. 4. Intervalley structure factor $S_{\text{IKS}}(\mathbf{Q})$ from HF and QMC at $\nu = -2$ with $N_{\mathbf{k}} = 18 \times 18$ and strain strength $\epsilon_s = 0.6\%$. (a) The HF solution has Bragg peaks corresponding to $\mathbf{q}_{\text{IKS}} = (7/18, 7/18)$. The magenta arrow points to the peak and is the same as those in Fig. 2 (d), (f), and (h). The brown rhombus is the mBZ and the cyan dot indicates $\mathbf{Q} = 0$. In (b), the IVC in the final HF density matrix has been artificially switched off when computing $S_{\text{IKS}}(\mathbf{Q})$. (c) $S_{\text{IKS}}(\mathbf{Q})$ from QMC.

Dirac points towards Γ_{M} , and Hartree renormalization [45–49], which generates a high energy peak there for $\nu < 0$. In terms of quantitative differences between the approximated QMC and HF, the occupation numbers in the QMC (panels (a) and (b)) do not reach as large a value compared to HF where $n^\eta(\mathbf{k}_{\text{max}}^\eta) = 2$. We attribute this observation to the fact that the approximated QMC nevertheless contains more fluctuation effects than HF.

To assess the relevance of IKS physics in greater detail, we introduce two additional ‘nesting’ diagnostics for IKS physics based on $n^\eta(\mathbf{k})$:

$$O'(\mathbf{q}) = \frac{1}{N_{\mathbf{k}}} \sum_{\mathbf{k}} n^+(\mathbf{k} + \mathbf{q}) (\bar{n} - n^-(\mathbf{k})), \quad (12)$$

$$O''(\mathbf{q}) = \max_{\mathbf{k}} |n^+(\mathbf{k} + \mathbf{q}) + n^-(\mathbf{k}) - \bar{n}| \geq 0. \quad (13)$$

For a mean-field IKS, $O''(\mathbf{q}_{\text{IKS}})$, which has been introduced previously in the DMRG study of Ref. [25], vanishes identically at the IKS wavevector. Hence, more generally, the value of \mathbf{q} at which $O''(\mathbf{q})$ reaches its minimum provides an estimate for the favored IVC wavevector \mathbf{q}_{IKS} . Similarly, for a mean-field IKS, $O'(\mathbf{q})$ is expected to be maximal at \mathbf{q}_{IKS} , since this is when the maximal occupation in one valley coincides with the minimal occupation in the other valley, and vice versa. The position of the maximum (minimum) of $O'(\mathbf{q})$ ($O''(\mathbf{q})$) therefore provides an estimate of the most favorable wavevector for IVC in the IKS ground state. Even if long-range IVC order is not strictly present, these nesting diagnostics can be viewed as predictions of the wavevector of a putative incipient IKS.

For $\epsilon_s = 0.6\%$, we find that the nesting diagnostics look qualitatively similar between QMC (Fig. 2 (e) and (g)) and HF (Fig. 2 (f) and (h)). In particular, the wavevector of the maximum (minimum) of $O'(\mathbf{q})$ ($O''(\mathbf{q})$), shown with magenta arrows, is consistent between the two calculations. The deviation of \mathbf{q}_{IKS} from these diagnostics compared to the simpler estimation $\mathbf{q}_{\text{IKS}} = \mathbf{k}_{\text{max}}^+ - \mathbf{k}_{\text{min}}^-$ from panels (c) and (d) is small, being within $< 20\%$ of the mBZ size. As expected, $O''(\mathbf{q})$ has a minimum of zero in the HF calculation. On the other hand,

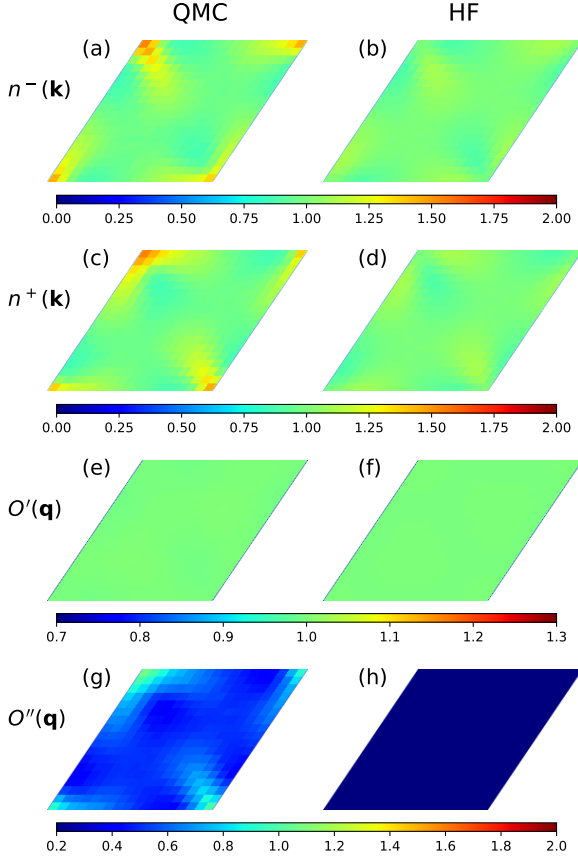


Fig. 5. Occupation number $n^\eta(\mathbf{k})$ and corresponding nesting diagnostics from QMC and HF at $\nu = -2$ with $N_{\mathbf{k}} = 18 \times 18$ and strain strength $\epsilon_s = 0$. The left panels are the QMC data, where (a) and (c) show the occupation factor $n^\eta(\mathbf{k})$. Panels (e) and (g) correspond to $O'(\mathbf{q})$ and $O''(\mathbf{q})$ respectively. The right panels are the corresponding data for the HF ground state which corresponds to a spin-polarized KIVC with $\mathbf{q} = 0$.

the corresponding diagnostic in QMC does not reach zero, but displays a significantly broadened minimum. This may be connected to the fact that the IKS wavevector is known to be soft in mean-field calculations [13], as shown explicitly in SI Fig. S3. Our conclusions are reproduced for a weaker strain strength of $\epsilon_s = 0.3\%$ in Fig. 3. Interestingly, we observe that the regions where QMC finds a large (small) value of $O'(\mathbf{q})$ ($O''(\mathbf{q})$) coincide with where HF can obtain an energetically competitive IKS solution (SI Fig. S3).

In a mean-field calculation, the one-body intervalley correlation function $\langle c_{s,+,\mathbf{k}+\mathbf{q},m}^\dagger c_{s,-,\mathbf{k},n} \rangle$ can develop a non-vanishing value in a $U(1)_v$ -breaking IVC state. However, in a QMC calculation, this expectation value identically vanishes since the many-body Hamiltonian preserves $U(1)_v$. The formation of long-range IVC order can instead be directly diagnosed by computing the intervalley structure factor

$$S_{ij}(\mathbf{Q}) = \frac{1}{N_{\mathbf{k}}} \langle \hat{O}_{ij}^\dagger(\mathbf{Q}) \hat{O}_{ij}(\mathbf{Q}) \rangle, \quad (14)$$

where we have defined the intervalley operator in the plane

wave basis

$$\begin{aligned} \hat{O}_{ij}(\mathbf{Q}) &= \sum_{\mathbf{k} \in \text{all}} \sum_{sll'\sigma\sigma'} \hat{c}_{s,+l,\sigma}^\dagger(\mathbf{k} + \mathbf{Q}) [\mu_i]_{ll'} [\sigma_j]_{\sigma\sigma'} \hat{c}_{s,-l',\sigma'}(\mathbf{k}). \end{aligned} \quad (15)$$

It is convenient to define $\hat{O}_{ij}(\mathbf{Q})$ in the plane wave basis since this avoids the phase ambiguity in the construction of the BM basis, i.e. in the gauge choice of $U_{\mathbf{k},m,\mathbf{G},l,\sigma}^{s,\eta}$ in Eq. (3). μ_i and σ_j are Pauli matrices in layer and sublattice spaces, respectively. We will mainly focus on the layer-sublattice channels $(i, j) = (2, 1), (0, 0)$, which are useful for detecting the KIVC and IKS respectively. Note that the KIVC symmetry-breaking order is invisible in the $(0, 0)$ channel due to its $\mathcal{T}' = \eta_y \mathcal{T}$ symmetry, while the IKS order is invisible in the $(2, 1)$ channel due to its \mathcal{T} symmetry. Hereafter $S_{2,1}$ and $S_{0,0}$ will be denoted as S_{KIVC} and S_{IKS} respectively. An IKS with spiral wavevector \mathbf{q}_{IKS} is expected to have ‘Bragg’ peaks in $S_{\text{IKS}}(\mathbf{q}_{\text{IKS}} + \mathbf{G})$. As $N_{\mathbf{k}} \rightarrow \infty$, the structure factor will be dominated by these Bragg peaks with finite amplitude, while other diffuse background features should decay to zero.

For $\epsilon_s = 0.6\%$, we show the intervalley structure factor for HF [Fig. 4 (a)] and QMC [Fig. 4 (c)]. As expected, the HF result exhibits strong peaks when \mathbf{Q} is equal to \mathbf{q}_{IKS} modulo a moiré RLV. In Fig. 4 (b), we isolate the diffuse background from Fig. 4 (a) by artificially switching off the IVC part of the self-consistent HF density matrix when computing $S_{\text{IKS}}(\mathbf{Q})$. In particular, this means that we set $P_{-,m;+,n}(\mathbf{k}, s) = P_{+,m;- ,n}(\mathbf{k}, s) = 0$ in the final converged density matrix. This procedure captures the effect of the IKS order on the renormalization of the flat bands, but effectively removes the long-range coherence. Interestingly, we find a close agreement between QMC (Fig. 4 (c)) and the diffuse background from HF (Fig. 4 (b)).

While the QMC structure factor does not exhibit intervalley Bragg peaks, the resemblance of the diffuse background of $S_{\text{IKS}}(\mathbf{Q})$ and the occupation number distribution with the mean-field IKS suggests that the QMC captures some key aspects of the physics related to the IKS phase. For instance, one possibility is that short-range correlations and interaction effects in the QMC have ‘primed’ the electrons to form intervalley electron-hole pairs, but long-range coherence is not yet established due to thermal/quantum fluctuations. Mean-field theory is expected to overestimate symmetry-breaking order, especially for phases that are not connected to an exact mean-field limit, and it could be that the true many-body ground state does not have proper IKS order for the parameters chosen here. Even within HF, the IKS manifold consists of multiple nearly-degenerate solutions with different \mathbf{q}_{IKS} (see SI Fig. S3), and this softness of the ordering wavevector could factor into the absence of the IKS peak in QMC. We comment that compared to the strong-coupling IVC states, the IKS in mean-field theory has a comparatively weaker total magnitude of IVC owing to its topologically-enforced momentum-space modulation. Another possibility is that the approximate QMC approach pursued here is fundamentally unable to capture peaks in the structure factor for the IKS.

We note that the single-particle Green’s function in the ap-

proximated QMC decays exponentially as a function of imaginary time for all \mathbf{k} (SI Fig. S4 [39]), implying a gapped insulating ground state from the electronic perspective. If the first scenario outlined above is applicable, then our results point towards a valley-disordered but charge-gapped state. In the second scenario, the fact that both approximated QMC and HF yield electronically-insulating states further suggests the interpretation of the IKS as consisting of a few auxiliary field configurations (a few Slater determinant states), whose one-particle properties can be captured with modified sampling weight, while it is the two-particle correlator, i.e. $S_{\text{IKS}}(\mathbf{q})$, that our approximated QMC might miss.

For comparison, we now consider the zero-strain limit as shown in Fig. 5, where the electron occupation distribution is significantly more homogeneous and mainly hovers around $n^l(\mathbf{k}) \approx 1$. In particular, the occupation does not approach 0 or 2. Furthermore, the nesting diagnostics in Eqs. (12)-(13) do not reveal any noticeable features. Indeed, the HF calculation yields a spin-polarized KIVC insulator instead of an IKS. In the QMC, the intervalley correlation function in the KIVC channel also suggests the interpretation as a KIVC state, as shown in Fig. S2 in SI [39]. We note that even without strain, the QMC simulation still suffers from the exponential sign problem, so that we continue to apply the approximation in Eq. (8) of taking the magnitude of the sampling weight. Nevertheless, the peak of the KIVC correlation function at $\mathbf{Q} = 0$ is consistently seen in QMC and HF.

III. DISCUSSION

The understanding of the rich phase diagram of the TBG, especially under the realistic situation with strain and away from the sign-problem-free charge neutrality point, is extremely difficult due to the exponential increase in the degrees of freedom involved. As a result, explanations of the experimentally observed insulating and superconducting states have largely been restricted to approximate or perturbative treatments. In the present context of $\nu = -2$, the IKS is not known to have an exactly solvable limit, so HF is not *a priori* as reliable (compared to, e.g., strong coupling states). Similarly, the arguments for topological constraints on the IVC need to be tested beyond mean-field level. Since the IKS exists in the ‘intermediate-coupling’ regime where kinetic energy and interactions compete on equal footing, more sophisticated approaches are required to reliably flesh out the phase diagram.

In this work, we have taken steps to achieve this by investigating the strain-induced IKS phase at filling factor $\nu = -2$ using a quantum many-body computational protocol consisting of momentum-space QMC, ED and HF. We approximated the sign problem in our continuous field momentum-space QMC simulation, and found that such treatment captures many aspects of the physics. In particular, the approximated QMC yields consistent electron occupation distributions and intervalley structure factors with ED for system sizes accessible with the latter. For larger systems, the QMC exhibits comparable electron occupations and IKS nesting diagnostics with the HF calculations. These results reflect the ‘intermediate-

coupling’ and the topologically constrained nature of the IKS state in a projected correlated flat-band setting.

We believe our combined protocol provides new routes towards understanding the many-body ground state of TBG in realistic settings. Our techniques may be generalized to non-integer fillings where HF has even less *a priori* justification for adequately capturing the relevant physics. In this doped regime, we expect that the approximated QMC can reveal further insights into the nature of the correlated and/or symmetry-broken metals, as well as the enigmatic superconductor. The QMC can also be utilized to examine finite-temperature physics [50, 51], such as the thermal disordering of the correlated states and energy scales of different elementary excitations in the system [51, 52]. We note that at finite temperature, the sign problem is less severe, and the approximated treatment eventually becomes exact, such that not only the single-particle Slater determinants but also the two-particle correlators such as the intervalley structure factors can be correctly captured. The temperature dependence of such physical observables will motivate a deeper investigation into the physical intuition and range of validity of the approximate QMC treatment and yield information about the thermal melting of KIVC, IKS, and other quantum many-body insulating ground states. Understanding such aspects will also enable applications of our combined protocol for other moiré systems beyond magic-angle twisted bilayer graphene.

Methods

Interacting continuum model of strained TBG.

We first describe the impact of uniaxial heterostrain and twisting on the moiré reciprocal lattice vectors of bilayer graphene. We represent the combined action of rotation and uniaxial straining on a single layer as [38]

$$\mathbb{T}(\theta, \epsilon_s, \phi_s) = (R(\theta) + S(\epsilon_s, \phi_s))^T, \quad (16)$$

where $R(\theta)$ denotes counter-clockwise rotation by angle θ . Let $\mathbf{G}_{1,2}^g$ denote the two unstrained and non-rotated basis reciprocal lattice vectors of graphene. Then, the moiré reciprocal lattice vectors for TBG with twist angle θ and uniaxial heterostrain (characterized by ϵ_s, ϕ_s) is

$$\mathbf{G}_{1,2}^m = \left(\mathbb{T}\left(\frac{\theta}{2}, \frac{\epsilon_s}{2}, \phi_s\right) - \mathbb{T}\left(-\frac{\theta}{2}, -\frac{\epsilon_s}{2}, \phi_s\right) \right) \mathbf{G}_{1,2}^g, \quad (17)$$

where $\mathbb{T}\left(\frac{\theta}{2}, \frac{\epsilon_s}{2}, \phi_s\right)$ and $\mathbb{T}\left(-\frac{\theta}{2}, -\frac{\epsilon_s}{2}, \phi_s\right)$ represent the rotation and straining of the upper ($l = 1$) and lower ($l = 2$) layers respectively. Similarly, the graphene BZ corners are rescaled as

$$\mathbf{K}_l^\eta = \mathbb{T}\left((-1)^{l+1}\frac{\theta}{2}, (-1)^{l+1}\frac{\epsilon_s}{2}, \phi_s\right) \left(\frac{|\mathbf{G}_1^g|}{\sqrt{3}}, 0 \right)^T \quad (18)$$

for each layer.

Hereafter, we use $\mathbf{G}_{1,2}$ to refer to the moiré reciprocal lattice vectors $\mathbf{G}_{1,2}^m$. The single-particle BM continuum Hamiltonian [53] can be constructed in the plane-wave basis as

$$\begin{aligned} H_0 &= \sum_{s,\eta,\mathbf{k},\mathbf{G},X,\mathbf{G}',X'} c_{s,\eta,X}^\dagger(\mathbf{k} + \mathbf{G}) (H_{\mathbf{k}}^{s,\eta})_{\mathbf{G},X,\mathbf{G}',X'} \\ &\quad \times c_{s,\eta,X}(\mathbf{k} + \mathbf{G}') \\ &= \sum_{s,\eta,\mathbf{k}} \vec{c}_{s,\eta}^\dagger(\mathbf{k}) H_{\mathbf{k}}^{s,\eta} \vec{c}_{s,\eta}(\mathbf{k}). \end{aligned} \quad (19)$$

Here $c_{s,\eta,X}^\dagger(\mathbf{k} + \mathbf{G})$ is the plane wave creation operator for spin s , valley η , and layer-sublattice index $X \in \{1A, 1B, 2A, 2B\}$. The plane wave momentum $\mathbf{k} + \mathbf{G}$ is decomposed into a part \mathbf{k} lying within the mBZ, and the remainder \mathbf{G} which lies on the moiré reciprocal lattice. $\vec{c}_{s,\eta}^\dagger(\mathbf{k})$ is a vector that collects $c_{s,\eta,X}^\dagger(\mathbf{k} + \mathbf{G})$ for all values of X and \mathbf{G} . Therefore, $H_{\mathbf{k}}^{s,\eta}$ is a $4N_{\mathbf{G}} \times 4N_{\mathbf{G}}$ matrix, where $N_{\mathbf{G}}$ is the number of plane waves retained within the momentum cutoff. In this work, a cutoff $|\mathbf{G}| \leq 6 \times \max\{|\mathbf{G}_1|, |\mathbf{G}_2|\}$ is applied. The matrix elements of $H_{\mathbf{k}}^{s,\eta}$ are

$$(H_{\mathbf{k}}^{s,\eta})_{\mathbf{G},\mathbf{G}'} = \delta_{\mathbf{G},\mathbf{G}'} \hbar v_F \begin{pmatrix} M_1^\eta & 0 \\ 0 & M_2^\eta \end{pmatrix} + \begin{pmatrix} 0 & T_1^{\eta\dagger} \\ T_2^{\eta\dagger} & 0 \end{pmatrix}. \quad (20)$$

The first term corresponds to the intralayer Dirac term where

$$M_l^\eta = -(\mathbf{k} + \mathbf{G} - \mathbf{A}_l^\eta - \mathbf{K}_l^\eta) \cdot \boldsymbol{\sigma}^\eta, \quad (21)$$

and $\boldsymbol{\sigma}^\eta = (\eta\sigma_x, \sigma_y)$ with σ_x, σ_y Pauli matrices in sublattice space. The vector potential

$$\mathbf{A}_l^\eta\left(\frac{\epsilon_s}{2}\right) = \eta \frac{3.14}{2a} \left(S\left(\frac{\epsilon_s}{2}\right)_{11} - S\left(\frac{\epsilon_s}{2}\right)_{22}, -2S\left(\frac{\epsilon_s}{2}\right)_{12} \right), \quad (22)$$

captures the shift of the monolayer Dirac points (in the absence of interlayer effects) from the rotated/strained graphene BZ corners \mathbf{K}_l^η . The second term of $H_{\mathbf{k}}^{s,\eta}$ encodes the interlayer tunneling processes according to

$$\begin{aligned} T_l^\eta &= \begin{pmatrix} u_0 & u_1 \\ u_1 & u_0 \end{pmatrix} \delta_{\mathbf{G},\mathbf{G}'} + \begin{pmatrix} u_0 & u_1 e^{-i\frac{2\pi}{3}\eta} \\ u_1 e^{i\frac{2\pi}{3}\eta} & u_0 \end{pmatrix} \delta_{\mathbf{G},\mathbf{G}'+(-1)^l\eta\mathbf{G}_1} \\ &\quad + \begin{pmatrix} u_0 & u_1 e^{i\frac{2\pi}{3}\eta} \\ u_1 e^{-i\frac{2\pi}{3}\eta} & u_0 \end{pmatrix} \delta_{\mathbf{G},\mathbf{G}'+(-1)^l\eta(\mathbf{G}_1+\mathbf{G}_2)}, \end{aligned} \quad (23)$$

where u_0 and u_1 are the same-sublattice and opposite-sublattice tunneling amplitudes respectively.

The long-range density-density interaction expressed in momentum space is

$$H_1 = \frac{1}{2\Omega} \sum_{\mathbf{q} \in \text{mBZ}, \mathbf{G}} V(\mathbf{q} + \mathbf{G}) \delta\rho_{\mathbf{q}+\mathbf{G}} \delta\rho_{-\mathbf{q}-\mathbf{G}}, \quad (24)$$

where

$$\begin{aligned} \delta\rho_{\mathbf{q}+\mathbf{G}} &= \sum_{s,\eta,\mathbf{k},\mathbf{G}',X'} c_{s,\eta,X'}^\dagger(\mathbf{k} + \mathbf{G}') c_{s,\eta,X'}(\mathbf{k} + \mathbf{q} + \mathbf{G} + \mathbf{G}') \\ &\quad - \frac{1}{2} \delta_{\mathbf{q},0} \delta_{\mathbf{G},0} \\ &= \sum_{s,\eta,\mathbf{k}} \left(\vec{c}_{s,\eta}^\dagger(\mathbf{k}) \vec{c}_{s,\eta}(\mathbf{k} + \mathbf{q} + \mathbf{G}) - \frac{1}{2} \delta_{\mathbf{q},0} \delta_{\mathbf{G},0} \right) \end{aligned} \quad (25)$$

is the electron density operator measured relative to a reference point that is charge neutral and featureless. Ω is the total real-space area of the system. For notational simplicity, from now on the momentum transfer $\mathbf{q} + \mathbf{G}$ is denoted as \mathbf{Q} .

We denote the eigenvalues and eigenvectors of the single-particle continuum model H_0 as $\epsilon_{\mathbf{k},m}^{s,\eta}$ and $|u_{\mathbf{k},m}^{s,\eta}\rangle$, satisfying $H_0 |u_{\mathbf{k},m}^{s,\eta}\rangle = \epsilon_{\mathbf{k},m}^{s,\eta} |u_{\mathbf{k},m}^{s,\eta}\rangle$, where m is a moiré band index. This can also be represented as the matrix equation

$$H_{\mathbf{k}}^{s,\eta} U_{\mathbf{k}}^{s,\eta} = U_{\mathbf{k}}^{s,\eta} E_{\mathbf{k}}^{s,\eta}, \quad (26)$$

where the m 'th column of $U_{\mathbf{k}}^{s,\eta}$ consists of the eigenvector for band m , and $E_{\mathbf{k}}^{s,\eta}$ is a diagonal matrix whose entries consist of the $\epsilon_{\mathbf{k},m}^{s,\eta}$. To express H_0 in the band basis, we first write

$$\begin{aligned} H_0 &= \sum_{s,\eta,\mathbf{k}} \vec{c}_{s,\eta}^\dagger(\mathbf{k}) H_{\mathbf{k}}^{s,\eta} \vec{c}_{s,\eta}(\mathbf{k}) \\ &= \sum_{s,\eta,\mathbf{k}} \vec{c}_{s,\eta}^\dagger(\mathbf{k}) U_{\mathbf{k}}^{s,\eta} E_{\mathbf{k}}^{s,\eta} U_{\mathbf{k}}^{s,\eta\dagger} \vec{c}_{s,\eta}(\mathbf{k}). \end{aligned} \quad (27)$$

We define the band basis operators

$$\vec{c}_{s,\eta,\mathbf{k}}^\dagger = \vec{c}_{s,\eta}^\dagger(\mathbf{k}) U_{\mathbf{k}}^{s,\eta}, \quad (28)$$

where the elements of $\vec{c}_{s,\eta,\mathbf{k}}$ are

$$c_{s,\eta,\mathbf{k},m}^\dagger = \sum_{\mathbf{G},X} U_{\mathbf{k},m,\mathbf{G},X}^{s,\eta} c_{s,\eta,X}^\dagger(\mathbf{k} + \mathbf{G}). \quad (29)$$

In this work, we work in the periodic gauge by imposing

$$[U_{\mathbf{k}+\mathbf{G}}^{s,\eta}]_{\mathbf{G}',X} = [U_{\mathbf{k}}^{s,\eta}]_{\mathbf{G}'+\mathbf{G},X}, \quad (30)$$

such that $|u_{\mathbf{k}+\mathbf{G},m}^{s,\eta}\rangle_{\mathbf{G}',X} = |u_{\mathbf{k},m}^{s,\eta}\rangle_{\mathbf{G}'+\mathbf{G},X}$ and $c_{s,\eta,\mathbf{k}+\mathbf{G},m} = c_{s,\eta,\mathbf{k},m}$. The single-particle continuum Hamiltonian is then recast as

$$\begin{aligned} H_0 &= \sum_{s,\eta,\mathbf{k}} \vec{c}_{s,\eta,\mathbf{k}}^\dagger E_{\mathbf{k}}^{s,\eta} \vec{c}_{s,\eta,\mathbf{k}} \\ &= \sum_{s,\eta,\mathbf{k},m} \epsilon_{\mathbf{k},m}^{s,\eta} c_{s,\eta,\mathbf{k},m}^\dagger c_{s,\eta,\mathbf{k},m}. \end{aligned} \quad (31)$$

The projection to the two low-energy bands (per spin and valley) is performed by keeping only the values of m corresponding to these bands. We find it convenient to further constrain the gauge of the BM Bloch functions of the central bands. We choose the relative gauge between the valleys so that \mathcal{PT} (which takes the form $\eta_x \mu_y \sigma_x$ in the plane wave basis) acts as $\eta_y n_y$ in the band basis with n_y acting on bands. In the ED calculations, we also fix the $C_2\mathcal{T}$ gauge (which acts in the plane wave basis according to $\sigma_x \mathcal{K}$, with \mathcal{K} complex conjugation) to make the form factor real.

We now rewrite the interaction term. Using the same transformation, we find

$$\begin{aligned} &\vec{c}_{s,\eta}^\dagger(\mathbf{k}) \vec{c}_{s,\eta}(\mathbf{k}+\mathbf{Q}) \\ &= \sum_{m,n} c_{s,\eta,\mathbf{k},m}^\dagger \left(U_{\mathbf{k}}^{s,\eta\dagger} U_{\mathbf{k}+\mathbf{Q}}^{s,\eta} \right)_{m,n} c_{s,\eta,\mathbf{k}+\mathbf{Q},n} \\ &= \sum_{m,n} c_{s,\eta,\mathbf{k},m}^\dagger \lambda_{m,n}^{s,\eta}(\mathbf{k}, \mathbf{Q}) c_{s,\eta,\mathbf{k}+\mathbf{Q},n}, \end{aligned} \quad (32)$$

where the form factor is defined as

$$\begin{aligned} \lambda_{m,n}^{s,\eta}(\mathbf{k}, \mathbf{Q}) &= \left(U_{\mathbf{k}}^{s,\eta\dagger} U_{\mathbf{k}+\mathbf{Q}}^{s,\eta} \right)_{m,n} \\ &= \langle u_{\mathbf{k},m}^{s,\eta} | u_{\mathbf{k}+\mathbf{Q},n}^{s,\eta} \rangle. \end{aligned} \quad (33)$$

This leads to

$$\delta\rho_{\mathbf{Q}} = \sum_{s,\eta,\mathbf{k}} \left(\sum_{m,n} \lambda_{m,n}^{s,\eta}(\mathbf{k}, \mathbf{Q}) c_{s,\eta,\mathbf{k},m}^\dagger c_{s,\eta,\mathbf{k}+\mathbf{Q},n} - \frac{1}{2} \delta_{\mathbf{Q},0} \delta_{\mathbf{G},0} \right). \quad (34)$$

Moreover, since

$$\begin{aligned} \delta_{\mathbf{G},0} &= \sum_m \langle u_{\mathbf{k},m}^{s,\eta} | u_{\mathbf{k}+\mathbf{G},m}^{s,\eta} \rangle \\ &= \sum_{m,n} \lambda_{m,n}^{s,\eta}(\mathbf{k}, \mathbf{G}) \delta_{m,n}, \end{aligned} \quad (35)$$

and

$$\delta_{\mathbf{Q},0} \delta_{\mathbf{G},0} = \sum_{m,n} \lambda_{m,n}^{s,\eta}(\mathbf{k}, \mathbf{Q}) \delta_{\mathbf{Q},0} \delta_{m,n}, \quad (36)$$

we have

$$\delta\rho_{\mathbf{Q}} = \sum_{s,\eta,\mathbf{k},m,n} \lambda_{m,n}^{s,\eta}(\mathbf{k}, \mathbf{Q}) \left(c_{s,\eta,\mathbf{k},m}^\dagger c_{s,\eta,\mathbf{k}+\mathbf{Q},n} - \frac{1}{2} \delta_{\mathbf{Q},0} \delta_{m,n} \right). \quad (37)$$

Similar to the procedure for the single-particle Hamiltonian H_0 , one method for implementing band projection for the interaction term H_I is to simply restrict the band indices to the central bands in $\delta\rho_{\mathbf{Q}}$. This corresponds to the ‘central average’ interaction scheme utilized in e.g. Refs. [15, 16]. We emphasize that the choice of interaction scheme is not unique (even when imposing constraints such as approximate many-body particle-hole symmetry). Within the projected Hamiltonian, different interaction schemes lead to different effective one-body corrections arising from the remote bands. Note that this interaction scheme differs from that used in Refs. [29, 30], where the last term in Eq. 37 depended on the target filling factor ν , which led to a polynomial instead of exponential sign problem at the chiral limit and at non-zero integer fillings in the absence of strain.

Since the set of momentum transfers has inversion symmetry, we can therefore write

$$\begin{aligned} H_I &= \sum_{|\mathbf{Q}| \neq 0} \frac{1}{2\Omega} V(\mathbf{Q}) \delta\rho_{\mathbf{Q}} \delta\rho_{-\mathbf{Q}} \\ &= \sum_{\mathbf{Q} > 0} \frac{1}{2\Omega} V(\mathbf{Q}) (\delta\rho_{\mathbf{Q}} \delta\rho_{-\mathbf{Q}} + \delta\rho_{-\mathbf{Q}} \delta\rho_{\mathbf{Q}}) \\ &= \sum_{\mathbf{Q} > 0} \frac{1}{4\Omega} V(\mathbf{Q}) \left((\delta\rho_{-\mathbf{Q}} + \delta\rho_{\mathbf{Q}})^2 - (\delta\rho_{-\mathbf{Q}} - \delta\rho_{\mathbf{Q}})^2 \right) \\ &= \sum_{\mathbf{Q} > 0} \frac{1}{4\Omega} V(\mathbf{Q}) \left(A_{\mathbf{Q}}^2 - B_{\mathbf{Q}}^2 \right), \end{aligned} \quad (38)$$

where the summation over momentum transfers $\mathbf{Q} > 0$ runs over half of the set of $\{\mathbf{Q}\}$ (i.e. only one of \mathbf{Q} or $-\mathbf{Q}$ is included). The $\mathbf{Q} = 0$ contribution can be absorbed into a tunable chemical potential term. The total Hamiltonian is then

$$H = H_0 + H_I - \mu \sum_{s,\eta,\mathbf{k},m} c_{s,\eta,\mathbf{k},m}^\dagger c_{s,\eta,\mathbf{k},m}, \quad (39)$$

where μ is used to adjust the average filling factor.

The continuous field quantum Monte Carlo algorithm

In this section, we discuss how to obtain the first line of Eq. 7 of the main text. We apply Trotter decomposition to evenly slice the partition function

$$\begin{aligned} Z &= \text{Tr} \left(e^{-\beta H} \right) = \text{Tr} \left(\prod_{\tau} e^{-\Delta\tau H} \right) \\ &= \text{Tr} \left(\prod_{\tau} \left(\prod_{\mathbf{Q}} \left(e^{-\frac{1}{2}\alpha(\mathbf{Q}) A_{\mathbf{Q}}^2} e^{\frac{1}{2}\alpha(\mathbf{Q}) B_{\mathbf{Q}}^2} \right) e^{-\Delta\tau H_0} \right) \right) \\ &\quad + \mathcal{O}(\alpha(\mathbf{Q} \rightarrow 0)), \end{aligned} \quad (40)$$

where $\beta = 1/(k_B T)$ with $k_B T = 0.167$ meV for $L = 18$. The imaginary time is $\tau \in [0, \beta]$ taken in steps of $\Delta\tau = \beta/600$. We have defined $\alpha(\mathbf{Q}) = \Delta\tau V(\mathbf{Q})/2\Omega$, where $\alpha(\mathbf{Q} \rightarrow 0) = 8 \times 10^{-3}$ for the simulation parameters used here. Then, we

decouple the interaction terms using the Gaussian integrals

$$e^{\frac{1}{2}\alpha(\mathbf{Q})(iA_{\mathbf{Q}})^2} = \frac{1}{\sqrt{2\pi}} \int_{-\infty}^{\infty} dx e^{-\frac{1}{2}x^2} e^{-ix\sqrt{\alpha(\mathbf{Q})}A_{\mathbf{Q}}} \quad (41)$$

$$e^{\frac{1}{2}\alpha(\mathbf{Q})B_{\mathbf{Q}}^2} = \frac{1}{\sqrt{2\pi}} \int_{-\infty}^{\infty} dx e^{-\frac{1}{2}x^2} e^{-x\sqrt{\alpha(\mathbf{Q})}B_{\mathbf{Q}}}, \quad (42)$$

with the auxiliary field x . Therefore, the partition function can be recast as

$$\begin{aligned} Z &= \int \left(\prod_{\tau, \mathbf{Q}} dx_{\tau, \mathbf{Q}, 1} dx_{\tau, \mathbf{Q}, 2} \right) e^{-\frac{1}{2} \sum_{\tau, \mathbf{Q}} (x_{\tau, \mathbf{Q}, 1}^2 + x_{\tau, \mathbf{Q}, 2}^2)} \\ &\times \text{Tr} \left(\prod_{\tau} e^{i \sum_{\mathbf{Q}} (-x_{\tau, \mathbf{Q}, 1} \sqrt{\alpha(\mathbf{Q})} A_{\mathbf{Q}} + i x_{\tau, \mathbf{Q}, 2} \sqrt{\alpha(\mathbf{Q})} B_{\mathbf{Q}})} e^{-\Delta \tau H_0} \right) \\ &+ \mathcal{O}(8 \times 10^{-3}). \end{aligned} \quad (43)$$

Note that the decoupling is exact, so that the error in Z above comes from the Trotter decomposition.

We apply Hamiltonian dynamics to update x . Rewrite the partition function as

$$\begin{aligned} Z &= \int \left(\prod_i dx_i dp_i \right) e^{-\frac{1}{2} \sum_i (x_i^2 + p_i^2)} \det(\mathbf{I} + B_C(\beta, 0)) \\ &+ \mathcal{O}(8 \times 10^{-3}), \end{aligned} \quad (44)$$

where the composite index $i \equiv (\tau, \mathbf{Q}, n)$ with $n = 1, 2$ is employed for compactness and an artificial momentum p_i is introduced for each x_i . $B_C(\beta, 0)$ is the matrix form of $\prod_{\tau} e^{i \sum_{\mathbf{Q}} (-x_{\tau, \mathbf{Q}, 1} \sqrt{\alpha(\mathbf{Q})} A_{\mathbf{Q}} + i x_{\tau, \mathbf{Q}, 2} \sqrt{\alpha(\mathbf{Q})} B_{\mathbf{Q}})} e^{-\Delta \tau H_0}$. C stands for a configuration of all the auxiliary fields $\{x_i, p_i\}$. The partition function can be further expressed as

$$Z = \int \left(\prod_i dx_i dp_i \right) e^{-\mathcal{H}} + \mathcal{O}(8 \times 10^{-3}), \quad (45)$$

with the effective Hamiltonian

$$\mathcal{H} \equiv \frac{1}{2} \sum_i (x_i^2 + p_i^2) - \ln(\det(\mathbf{I} + B_C(\beta, 0))). \quad (46)$$

The Hamiltonian dynamics is applied as

$$\begin{aligned} \frac{dp_i}{dt} &= - \frac{\partial \mathcal{H}}{\partial x_i} \\ &= -x_i + 2 \sum_{\eta} \text{Tr} \left(J_{\mathbf{Q}}^{\eta} (\mathbf{I} - G^{\eta}(\tau)) \right) + \mathcal{O}(10^{-2}) \end{aligned} \quad (47)$$

$$\begin{aligned} \frac{dx_i}{dt} &= \frac{\partial \mathcal{H}}{\partial p_i} \\ &= p_i, \end{aligned}$$

where $G^{\eta}(\tau)$ is the equal-time Green's function for $s = \uparrow$, and $J_{\mathbf{Q}}^{\eta}$ is the matrix form of $A_{\mathbf{Q}}^{\eta}$ or $B_{\mathbf{Q}}^{\eta}$ for $n = 1$ or 2 . The Hamiltonian dynamics facilitates increased acceptance rates through

the conservation of the Hamiltonian along equal-energy trajectories. The Metropolis-Hastings scheme is used to determine acceptance or rejection of the update of x_i .

The partition function can also be written as

$$\begin{aligned} Z &= \int \left(\prod_i dx_i dp_i \right) W_C \\ &= \int dC W_C, \end{aligned} \quad (48)$$

where $W_C = e^{-\mathcal{H}}$ is generally a complex number. An observable \hat{O} can thus be measured by

$$\langle \hat{O} \rangle = \frac{\int dC O_C W_C}{\int dC W_C}, \quad (49)$$

with O_C the value of \hat{O} in C . Thus, we have derived Eq. 7 in the main text. In the main text, we discuss the approximated QMC framework which does not have a sign problem (see Eq. 8). In SI Sec. S5, we discuss the symmetry properties of the approximated QMC.

Exact Diagonalization

For the exact diagonalization calculations, we consider both valleys and restrict to a single spin sector. Since we employ product (Fock) states with definite particle number, the chemical potential term μ is not needed. The Hamiltonian can be expressed as

$$H = E_0 + \sum_i V_0(i) c_i^{\dagger} c_i + \sum_{i \neq j} V_1(i, j) c_i^{\dagger} c_i c_j^{\dagger} c_j + H_1, \quad (50)$$

where

$$\begin{aligned} H_1 &= \sum_{i > j} V_2(i, j) c_i^{\dagger} c_j + \sum_{i > j, k} V_3(i, j, k) c_i^{\dagger} c_j c_k^{\dagger} c_k \\ &+ \sum_{i > j > k > l} \left(V_4(i, j, k, l) c_i^{\dagger} c_j c_k c_l^{\dagger} + V_5(i, j, k, l) c_i^{\dagger} c_j c_k^{\dagger} c_l \right) \\ &+ \sum_{i > j > k > l} V_6(i, j, k, l) c_i^{\dagger} c_j^{\dagger} c_k c_l + h.c.. \end{aligned} \quad (51)$$

A product state is

$$\begin{aligned} |\vec{z}\rangle &= c_{i_1}^{\dagger} c_{i_2}^{\dagger} \cdots c_{i_N}^{\dagger} |0\rangle \\ &= |0 \ 1 \ 0 \ 0 \ 1 \ \cdots \ 1 \ 0\rangle, \end{aligned} \quad (52)$$

where $|0\rangle$ consists of $4N_{\mathbf{k}}$ bits of 0 and $N = N_{\mathbf{k}}$ corresponds to the particle number at filling $\nu = -1$ (i.e. $\nu = -2$ in the spinful calculation). $i_i \in [1, 4N_{\mathbf{k}}]$ is a composite index for $c_{\eta, \mathbf{k}, m}^{\dagger}$, and $i_1 > i_2 > \cdots > i_N$. In this basis, the diagonal elements of H are

$$H_{i_i} = \sum_{|\vec{z}\rangle_{i_i=1}} V_0(i) + \sum_{|\vec{z}\rangle_{i=|\vec{z}\rangle_{j=1}} V_1(i, j), \quad (53)$$

where $|\dot{i}\rangle_i$ stands for the i^{th} element of $|\dot{i}\rangle$. The elements $H_{i,j}$

of the lower-triangular part of H are

$$\begin{aligned}
& \sum_{\{i>j, |\dot{i}\rangle_i=0, |\dot{j}\rangle_j=1\}} (-1)^{\zeta(i,j)} V_2(i, j) \\
& + \sum_{\{i>j, |\dot{i}\rangle_i=0, |\dot{j}\rangle_j=|\dot{k}\rangle_k=1\}} (-1)^{\zeta(i,j)} V_3(i, j, k) \\
& + \sum_{\{i>j>k>l, |\dot{i}\rangle_i=|\dot{j}\rangle_l=0, |\dot{j}\rangle_j=|\dot{k}\rangle_k=1\}} (-1)^{\zeta(i,j)+\zeta(k,l)} V_4(i, j, k, l) \\
& + \sum_{\{i>j>k>l, |\dot{i}\rangle_i=|\dot{j}\rangle_k=0, |\dot{j}\rangle_j=|\dot{k}\rangle_l=1\}} (-1)^{\zeta(i,j)+\zeta(k,l)} V_5(i, j, k, l) \\
& + \sum_{\{i>j>k>l, |\dot{i}\rangle_i=|\dot{j}\rangle_j=0, |\dot{j}\rangle_k=|\dot{k}\rangle_l=1\}} (-1)^{\zeta(i,j)+\zeta(k,l)} V_6(i, j, k, l),
\end{aligned} \tag{54}$$

where $\zeta(i, j)$ is the number of ‘1’s that occur in the range $[i, j)$. The upper-triangular elements of H can be obtained by Hermiticity. H conserves total moiré momentum \mathbf{k} and valley charge, so that we can diagonalize these smaller symmetry sub-blocks to obtain eigenvalues and eigenvectors.

Data availability

The data generated in this study are provided in the Supplementary Information file.

-
- [1] Y. Cao, V. Fatemi, A. Demir, S. Fang, S. L. Tomarken, J. Y. Luo, J. D. Sanchez-Yamagishi, K. Watanabe, T. Taniguchi, E. Kaxiras, R. C. Ashoori, and P. Jarillo-Herrero, Correlated insulator behaviour at half-filling in magic-angle graphene superlattices, *Nature* **556**, 80–84 (2018).
- [2] Y. Cao, V. Fatemi, S. Fang, K. Watanabe, T. Taniguchi, E. Kaxiras, and P. Jarillo-Herrero, Unconventional superconductivity in magic-angle graphene superlattices, *Nature* **556**, 43–50 (2018).
- [3] A. Kerelsky, L. J. McGilly, D. M. Kennes, L. Xian, M. Yankowitz, S. Chen, K. Watanabe, T. Taniguchi, J. Hone, C. Dean, et al., Maximized electron interactions at the magic angle in twisted bilayer graphene, *Nature* **572**, 95 (2019).
- [4] Y. Choi, J. Kemmer, Y. Peng, A. Thomson, H. Arora, R. Polski, Y. Zhang, H. Ren, J. Alicea, G. Refael, et al., Electronic correlations in twisted bilayer graphene near the magic angle, *Nature physics* **15**, 1174 (2019).
- [5] Y. Xie, B. Lian, B. Jäck, X. Liu, C.-L. Chiu, K. Watanabe, T. Taniguchi, B. A. Bernevig, and A. Yazdani, Spectroscopic signatures of many-body correlations in magic-angle twisted bilayer graphene, *Nature* **572**, 101 (2019).
- [6] D. Wong, K. P. Nuckolls, M. Oh, B. Lian, Y. Xie, S. Jeon, K. Watanabe, T. Taniguchi, B. A. Bernevig, and A. Yazdani, Cascade of electronic transitions in magic-angle twisted bilayer graphene, *Nature* **582**, 198 (2020).
- [7] N. P. Kazmierczak, M. Van Winkle, C. Ophus, K. C. Bustillo, S. Carr, H. G. Brown, J. Ciston, T. Taniguchi, K. Watanabe, and D. K. Bediako, Strain fields in twisted bilayer graphene, *Nature materials* **20**, 956 (2021).
- [8] L. Huder, A. Artaud, T. Le Quang, G. T. de Laissardière, A. G. M. Jansen, G. Lapertot, C. Chapelier, and V. T. Renard, Electronic spectrum of twisted graphene layers under heteros-train, *Phys. Rev. Lett.* **120**, 156405 (2018).
- [9] F. Mesple, A. Missaoui, T. Cea, L. Huder, F. Guinea, G. Trambly de Laissardière, C. Chapelier, and V. T. Renard, Heterostrain determines flat bands in magic-angle twisted graphene layers, *Phys. Rev. Lett.* **127**, 126405 (2021).
- [10] D. E. Parker, T. Soejima, J. Hauschild, M. P. Zaletel, and N. Bultinck, Strain-induced quantum phase transitions in magic-angle graphene, *Phys. Rev. Lett.* **127**, 027601 (2021).
- [11] K. P. Nuckolls, R. L. Lee, M. Oh, D. Wong, T. Soejima, J. P. Hong, D. Călugăru, J. Herzog-Arbeitman, B. A. Bernevig, K. Watanabe, et al., Quantum textures of the many-body wavefunctions in magic-angle graphene, *Nature* **620**, 525 (2023).
- [12] H. Kim, Y. Choi, E. Lantagne-Hurtubise, C. Lewandowski, A. Thomson, L. Kong, H. Zhou, E. Baum, Y. Zhang, L. Holleis, K. Watanabe, T. Taniguchi, A. F. Young, J. Alicea, and S. Nadj-Perge, Imaging inter-valley coherent order in magic-angle twisted trilayer graphene, *Nature* **623**, 942 (2023).
- [13] Y. H. Kwan, G. Wagner, T. Soejima, M. P. Zaletel, S. H. Simon, S. A. Parameswaran, and N. Bultinck, Kekulé spiral order at all nonzero integer fillings in twisted bilayer graphene, *Phys. Rev. X* **11**, 041063 (2021).
- [14] G. Wagner, Y. H. Kwan, N. Bultinck, S. H. Simon, and S. A. Parameswaran, Global phase diagram of the normal state of twisted bilayer graphene, *Phys. Rev. Lett.* **128**, 156401 (2022).
- [15] N. Bultinck, E. Khalaf, S. Liu, S. Chatterjee, A. Vishwanath, and M. P. Zaletel, Ground state and hidden symmetry of magic-angle graphene at even integer filling, *Phys. Rev. X* **10**, 031034 (2020).
- [16] B. Lian, Z.-D. Song, N. Regnault, D. K. Efetov, A. Yazdani, and B. A. Bernevig, Twisted bilayer graphene. iv. exact insulator ground states and phase diagram, *Phys. Rev. B* **103**, 205414 (2021).
- [17] J. Kang and O. Vafek, Strong coupling phases of partially filled

- twisted bilayer graphene narrow bands, *Phys. Rev. Lett.* **122**, 246401 (2019).
- [18] Y. Da Liao, J. Kang, C. N. Breiø, X. Y. Xu, H.-Q. Wu, B. M. Andersen, R. M. Fernandes, and Z. Y. Meng, Correlation-induced insulating topological phases at charge neutrality in twisted bilayer graphene, *Phys. Rev. X* **11**, 011014 (2021).
- [19] P. J. Ledwith, E. Khalaf, and A. Vishwanath, Strong coupling theory of magic-angle graphene: A pedagogical introduction, *Annals of Physics* **435**, 168646 (2021), special issue on Philip W. Anderson.
- [20] J. Herzog-Arbeitman, J. Yu, D. Călugăru, H. Hu, N. Regnault, O. Vafek, J. Kang, and B. A. Bernevig, Topological heavy fermion model as an efficient representation of atomistic strain and relaxation in twisted bilayer graphene, *Phys. Rev. B* **112**, 125128 (2025).
- [21] J. Herzog-Arbeitman, D. Călugăru, H. Hu, J. Yu, N. Regnault, J. Kang, B. A. Bernevig, and O. Vafek, Kekulé spiral order from strained topological heavy fermions, *Phys. Rev. B* **112**, 125129 (2025).
- [22] Z. Song, Z. Wang, W. Shi, G. Li, C. Fang, and B. A. Bernevig, All magic angles in twisted bilayer graphene are topological, *Phys. Rev. Lett.* **123**, 036401 (2019).
- [23] J. Ahn, S. Park, and B.-J. Yang, Failure of nielsen-ninomiya theorem and fragile topology in two-dimensional systems with space-time inversion symmetry: Application to twisted bilayer graphene at magic angle, *Phys. Rev. X* **9**, 021013 (2019).
- [24] Y. H. Kwan, Z. Wang, G. Wagner, S. H. Simon, S. A. Parameswaran, and N. Bultinck, Textured exciton insulators, *Phys. Rev. B* **112**, 035129 (2025).
- [25] T. Wang, D. E. Parker, T. Soejima, J. Hauschild, S. Anand, N. Bultinck, and M. P. Zaletel, Ground-state order in magic-angle graphene at filling $\nu = -3$: A full-scale density matrix renormalization group study, *Phys. Rev. B* **108**, 235128 (2023).
- [26] C. Huang, N. Parthenios, M. Ulybyshev, X. Zhang, F. F. Assaad, L. Classen, and Z. Y. Meng, Angle-tuned gross-neveu quantum criticality in twisted bilayer graphene, *Nature Communications* **16**, 7176 (2025).
- [27] X. Zhang, G. Pan, Y. Zhang, J. Kang, and Z. Y. Meng, Momentum space quantum monte carlo on twisted bilayer graphene, *Chinese Physics Letters* **38**, 077305 (2021).
- [28] J. S. Hofmann, E. Khalaf, A. Vishwanath, E. Berg, and J. Y. Lee, Fermionic monte carlo study of a realistic model of twisted bilayer graphene, *Phys. Rev. X* **12**, 011061 (2022).
- [29] X. Zhang, G. Pan, X. Y. Xu, and Z. Y. Meng, Fermion sign bounds theory in quantum monte carlo simulation, *Phys. Rev. B* **106**, 035121 (2022).
- [30] X. Zhang, G. Pan, B.-B. Chen, H. Li, K. Sun, and Z. Y. Meng, Polynomial sign problem and topological mott insulator in twisted bilayer graphene, *Phys. Rev. B* **107**, L241105 (2023).
- [31] C. Huang, X. Zhang, G. Pan, H. Li, K. Sun, X. Dai, and Z. Y. Meng, Evolution from quantum anomalous hall insulator to heavy-fermion semimetal in magic-angle twisted bilayer graphene, *Phys. Rev. B* **109**, 125404 (2024).
- [32] G. Pan and Z. Y. Meng, The sign problem in quantum monte carlo simulations, in *Encyclopedia of Condensed Matter Physics (Second Edition)*, edited by T. Chakraborty (Academic Press, Oxford, 2024) second edition ed., pp. 879–893.
- [33] R. Bistritzer and A. H. MacDonald, Moiré bands in twisted double-layer graphene, *Proceedings of the National Academy of Sciences* **108**, 12233 (2011).
- [34] S. Carr, S. Fang, Z. Zhu, and E. Kaxiras, Exact continuum model for low-energy electronic states of twisted bilayer graphene, *Phys. Rev. Res.* **1**, 013001 (2019).
- [35] M. Koshino, N. F. Q. Yuan, T. Koretsune, M. Ochi, K. Kuroki, and L. Fu, Maximally localized wannier orbitals and the extended hubbard model for twisted bilayer graphene, *Phys. Rev. X* **8**, 031087 (2018).
- [36] N. N. T. Nam and M. Koshino, Lattice relaxation and energy band modulation in twisted bilayer graphene, *Phys. Rev. B* **96**, 075311 (2017).
- [37] O. Vafek and J. Kang, Renormalization group study of hidden symmetry in twisted bilayer graphene with coulomb interactions, *Phys. Rev. Lett.* **125**, 257602 (2020).
- [38] Z. Bi, N. F. Q. Yuan, and L. Fu, Designing flat bands by strain, *Phys. Rev. B* **100**, 035448 (2019).
- [39] The free dispersions under strain, the comparison of structure factors between QMC and HF, the HF energy as a function of \mathbf{q}_{IKS} , single-particle Green's function in QMC, and the properties of the approximated QMC are given in this Supplemental Information.
- [40] F. Xie, A. Cowsik, Z.-D. Song, B. Lian, B. A. Bernevig, and N. Regnault, Twisted bilayer graphene. vi. an exact diagonalization study at nonzero integer filling, *Phys. Rev. B* **103**, 205416 (2021).
- [41] P. Potasz, M. Xie, and A. H. MacDonald, Exact diagonalization for magic-angle twisted bilayer graphene, *Phys. Rev. Lett.* **127**, 147203 (2021).
- [42] Y. H. Kwan, Z. Wang, G. Wagner, N. Bultinck, S. H. Simon, and S. A. Parameswaran, Mean-field modeling of moiré materials: a user's guide with selected applications to twisted bilayer graphene, *Advances in Physics* **0**, 1 (2025), <https://doi.org/10.1080/00018732.2025.2600658>.
- [43] Z. Wang, G. Wagner, Y. H. Kwan, N. Bultinck, S. H. Simon, and S. A. Parameswaran, Putting a new spin on the incommensurate kekulé spiral: from spin-valley locking and collective modes to fermiology and implications for superconductivity (2025), arXiv:2509.12320 [cond-mat.str-el].
- [44] Z. Wang, Y. H. Kwan, G. Wagner, S. H. Simon, N. Bultinck, and S. A. Parameswaran, Chern-textured exciton insulators with valley spiral order in moiré materials, *Phys. Rev. B* **112**, 035130 (2025).
- [45] F. Guinea and N. R. Walet, Electrostatic effects, band distortions, and superconductivity in twisted graphene bilayers, *Proceedings of the National Academy of Sciences* **115**, 13174 (2018).
- [46] L. Rademaker, D. A. Abanin, and P. Mellado, Charge smoothening and band flattening due to hartree corrections in twisted bilayer graphene, *Phys. Rev. B* **100**, 205114 (2019).
- [47] T. Cea, N. R. Walet, and F. Guinea, Electronic band structure and pinning of fermi energy to van hove singularities in twisted bilayer graphene: A self-consistent approach, *Phys. Rev. B* **100**, 205113 (2019).
- [48] Z. A. H. Goodwin, V. Vitale, X. Liang, A. A. Mostofi, and J. Lischner, Hartree theory calculations of quasiparticle properties in twisted bilayer graphene (2020), arXiv:2004.14784 [cond-mat.mes-hall].
- [49] J. Kang, B. A. Bernevig, and O. Vafek, Cascades between light and heavy fermions in the normal state of magic angle twisted bilayer graphene (2021), arXiv:2104.01145 [cond-mat.str-el].
- [50] X. Zhang, K. Sun, H. Li, G. Pan, and Z. Y. Meng, Superconductivity and bosonic fluid emerging from moiré flat bands, *Phys. Rev. B* **106**, 184517 (2022).
- [51] G. Pan, X. Zhang, H. Lu, H. Li, B.-B. Chen, K. Sun, and Z. Y. Meng, Thermodynamic characteristic for a correlated flat-band system with a quantum anomalous hall ground state, *Phys. Rev. Lett.* **130**, 016401 (2023).
- [52] X. Lin, B.-B. Chen, W. Li, Z. Y. Meng, and T. Shi, Exciton proliferation and fate of the topological mott insulator in a twisted

- bilayer graphene lattice model, *Phys. Rev. Lett.* **128**, 157201 (2022).
- [53] R. Bistritzer and A. H. MacDonald, Moiré bands in twisted double-layer graphene, *Proceedings of the National Academy of Sciences* **108**, 12233 (2011).
- [54] HPC2021, Information Technology Services, The University of Hong Kong .
- [55] Beijing PARATERA Tech CO.,Ltd .
- [56] T. Grover, Entanglement of interacting fermions in quantum monte carlo calculations, *Phys. Rev. Lett.* **111**, 130402 (2013).
- [57] M. Ulybyshev and F. F. Assaad, Beyond the instanton gas approach: dominant thimbles approximation for the Hubbard model, *arXiv e-prints* , arXiv:2407.09452 (2024), arXiv:2407.09452 [cond-mat.str-el].

Acknowledgments

We acknowledge discussions with Nikolaos Parthenios and Jeyong Park on similar topics. C.H. and Z.Y.M. acknowledge the support from the Research Grants Council (RGC) of Hong Kong Special Administrative Region (SAR) of China (Project Nos. AoE/P701/20, C7037-22GF, 17302223, 17301924, 17301725), the ANR/RGC Joint Research Scheme sponsored by RGC of Hong Kong and French National Research Agency (Project No. A_HKU703/22) and the State Key Laboratory of Optical Quantum Materials at HKU. C.H. and Z.Y.M thank HPC2021 system under the Information Technology Services at the University of Hong Kong [54], as well as the Beijing Paratera Tech Corp., Ltd [55] for providing HPC resources that have contributed to the research results reported within this paper. L.C. was funded by the European Union (ERC-2023-STG, Project 101115758 - QuantEmerge). MU acknowledges support by the Deutsche Forschungsgemeinschaft through AS 120/19-1 (Project No. 530989922). FFA acknowledges support by the Würzburg-Dresden Cluster of Excellence *ctd.qmat* (EXC 2147, Project No. 390858490).

Supplemental Information for "Strain-Tuned Incommensurate Kekulé Spiral (IKS) Order in Twisted Bilayer Graphene: a Quantum Many-Body Investigation"

In this Supplemental Information, we discuss the non-interacting dispersion for different strain strengths in Sec. S1. We provide additional data for the intervalley structure factors at zero and finite strains in Sec. S2. In Sec. S3, we show the energy landscape of IKS states within HF, illustrating the softness of the ordering wavevector within mean-field theory. In Sec. S4, we show the single-particle Green's function within approximated QMC with and without strain, and find in both cases that the system is an insulator with a single-particle gap. In Sec. S5, we demonstrate that the approximated QMC preserves the symmetries of the original Hamiltonian, and discuss the Hermiticity of the approximated Hamiltonian.

S1. DISPERSION FOR DIFFERENT STRAIN STRENGTHS

The dispersion of non-interacting Hamiltonian $H_{\mathbf{k}}^{s,\eta}$ for $s = \uparrow$ and $\eta = +$ is shown in Supplementary Fig. S1 with various strain strengths ϵ_s , where the inflation of the bandwidth of two low-energy bands and the shifting of the deformed Dirac cones from the mBZ corners are seen.

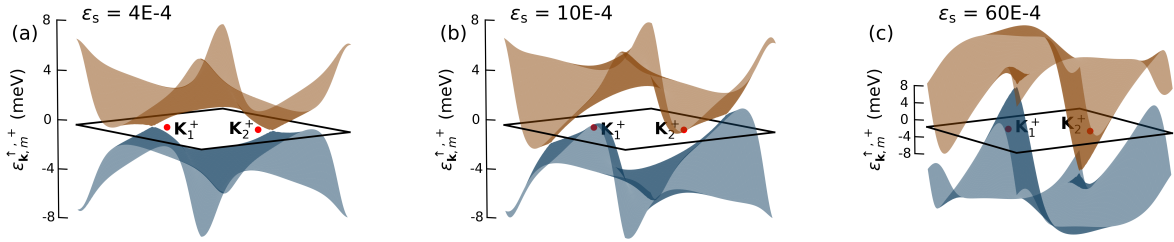


Fig. S1. **Evolution of the non-interacting dispersion with the strain strength ϵ_s .** Note that $\theta = 1.15^\circ$, $\phi_s = 130^\circ$, $u_0 = 80$ meV, and the moiré Brillouin zone is denoted by the black rhombus. Red dots stand for the moiré Brillouin zone corners \mathbf{K}_1^+ and \mathbf{K}_2^+ . Different dispersion colors are used to indicate distinct bands.

S2. INTERVALLEY COHERENCE STRUCTURE FACTORS

In this section we show the comparisons of the KIVC structure factor S_{KIVC} and IKS structure factor S_{IKS} from both approximated QMC and HF at $\epsilon_s = 0$ and $\epsilon_s = 0.6\%$ in Supplementary Fig. S2. The definitions of these structure factors are given in the main text.

In QMC, a KIVC peak at $\mathbf{q} = 0$ is detected in Supplementary Fig. S2 (a), while the IKS structure factor does not exhibit a peak as shown in Supplementary Fig. S2 (b). When a strain of $\epsilon_s = 0.6\%$ turned on, the KIVC order vanishes as no peak appears in (c), while the IKS structure factor develops sizable weight in the vicinity of \mathbf{q}_{IKS} in (d). However, $S_{\text{IKS}}(\mathbf{q})$ does not exhibit a peak that survives for increasing L .

In HF, a strong KIVC peak is seen at $\mathbf{q} = 0$ without strain in Fig. S2 (e), while strong IKS peaks at $\mathbf{q} = \mathbf{q}_{\text{IKS}} + \mathbf{G}$ are resolved at $\epsilon_s = 0.6\%$ in Fig. S2 (h). At zero strain (finite strain $\epsilon_s = 0.6\%$), no IKS (KIVC) order is observed.

S3. ADDITIONAL HARTREE-FOCK RESULTS

In Fig. S3, we perform HF calculations with the parameters used in Figs. 2 and 3. Recall that in the HF procedure, we perform calculations for all possible values of intervalley spiral moiré wavevector \mathbf{q} lying on the momentum mesh. For a large portion of such \mathbf{q} , the lowest energy HF state corresponds to an IKS state. In Fig. S3, we show the energy of these IKS states as a function of \mathbf{q}_{IKS} , measured relative to the global ground state IKS (i.e. the IKS with the lowest energy across all possible \mathbf{q}_{IKS}). For both values of strain $\epsilon_s = 0.3, 0.6\%$, we find that the landscape of IKS states is energetically very soft. For example, IKS states with an \mathbf{q}_{IKS} that differs by half a RLV compared to the value of \mathbf{q}_{IKS} in the global ground state can still be within 0.5 meV per unit cell. We also find that the region of \mathbf{q}_{IKS} with low-lying IKS states qualitatively resembles the region where $O''(\mathbf{q})$ is small in the QMC calculations of Figs. 2 and 3. The close competition between many different IKS states could be relevant for the inability for approximated QMC to resolve a long-range-ordered IKS, at least for these parameters, since the softness of the energy for different \mathbf{q}_{IKS} points to strong fluctuations around the mean-field ground state.

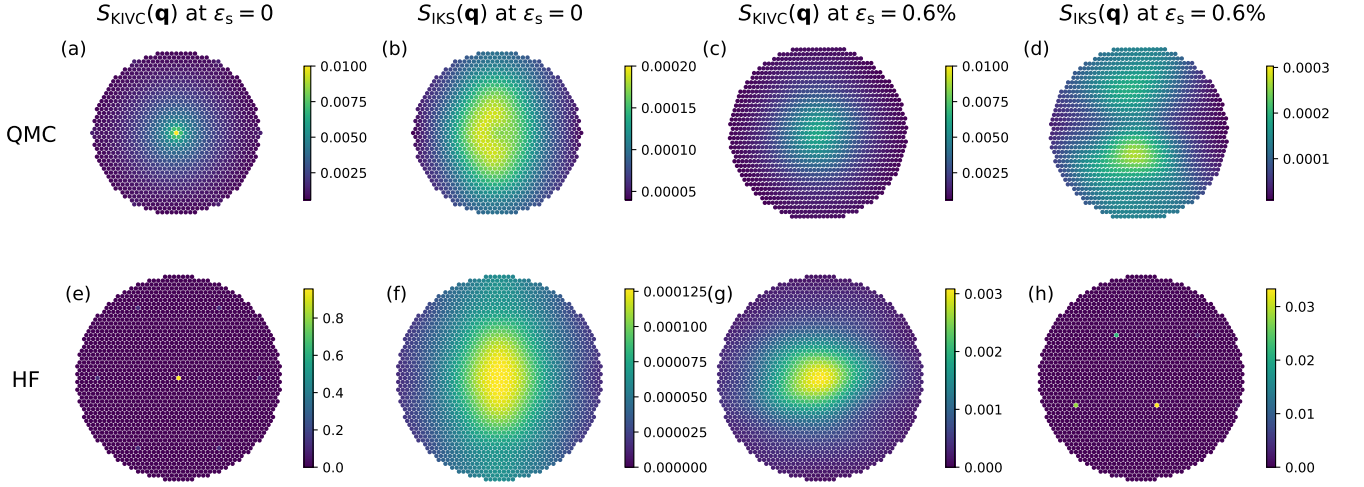


Fig. S2. **Comparisons of KIVC and IKS structure factors from QMC and HF at $\nu = -2$ with $N_{\mathbf{k}} = 18 \times 18$.** Upper panels are from approximated QMC while the lower ones are from HF. $S_{\text{KIVC}}(\mathbf{q})$ with zero strain is shown in (a) and (e), and with 0.6% is shown in (c) and (g). $S_{\text{IKS}}(\mathbf{q})$ with zero strain is shown in (b) and (f), and with 0.6% is shown in (d) and (h). $\mathbf{q} = 0$ is located at the center of each plot. Model parameters are $\theta = 1.15^\circ$, $\phi_s = 130^\circ$, $u_0 = 80$ meV and $\epsilon_r = 10$.

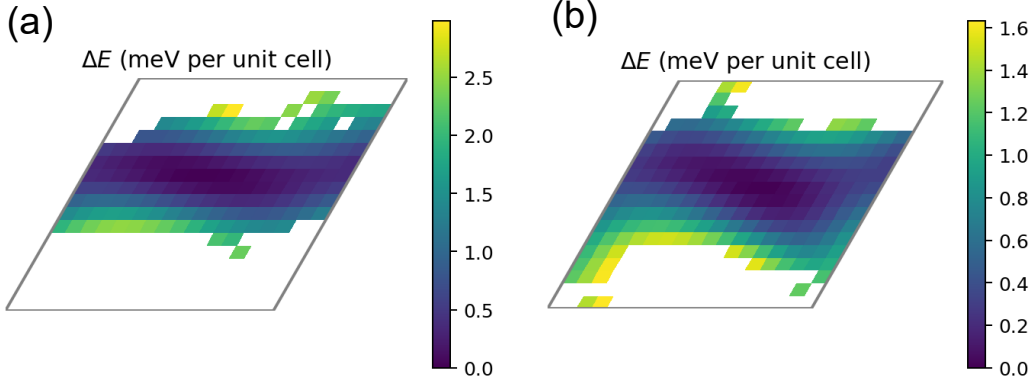


Fig. S3. **HF energy of IKS states as a function of \mathbf{q}_{IKS} at $\nu = -2$ with $N_{\mathbf{k}} = 18 \times 18$.** We consider strain strength $\epsilon_s = 0.6\%$ in (a) and $\epsilon_s = 0.3\%$ in (b). The energy ΔE is measured relative to the ground state taken across all \mathbf{q}_{IKS} . White regions indicate values of \mathbf{q} where HF did not obtain a time-reversal symmetric IKS. Model parameters are $\theta = 1.15^\circ$, $\phi_s = 130^\circ$, $u_0 = 80$ meV and $\epsilon_r = 10$.

S4. SINGLE-PARTICLE GREEN'S FUNCTIONS

In this section, we show that the interacting system for $\epsilon_s = 0.0\%, 0.6\%$ in approximated QMC is gapped by monitoring the imaginary time single-particle Green's function in Supplementary Fig. S4. The Green's functions were calculated for the system size of $L = 12$ and the temperature of $\beta = 0.25$ meV. For all the \mathbf{k} points in the mBZ, the $G_{\mathbf{k}}(\tau)$ all decay quickly to 0 as a function of imaginary time for both strains. Such decay implies that the single-particle spectrum is gapped at all the momenta considered and hence the system is an insulator from the electronic perspective.

S5. PROPERTIES OF APPROXIMATED QMC

We consider the Hamiltonian

$$\hat{H} = \sum_{s,\eta,\mathbf{k},m} \left(\epsilon_{\mathbf{k},m}^{s,\eta} - \mu \right) c_{s,\eta,\mathbf{k},m}^\dagger c_{s,\eta,\mathbf{k},m} + \sum_{\mathbf{Q}>0} \frac{1}{4\Omega} V(\mathbf{Q}) \left(A_{\mathbf{Q}}^2 - B_{\mathbf{Q}}^2 \right), \quad (\text{S55})$$

which generally possesses a sign problem in the auxiliary field QMC method. The question we address here is whether there is a proximate Hamiltonian that shares the same symmetries of those of the original Hamiltonian, but is free of the negative sign

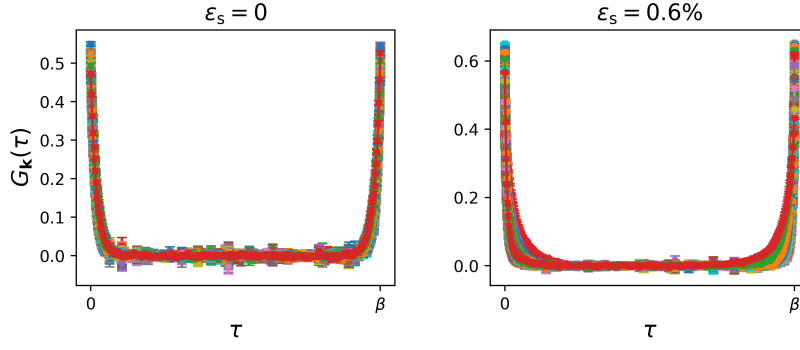


Fig. S4. **Single-particle Green's functions at $\epsilon_s = 0$ and 0.6%** for $L = 12$ within approximated QMC. Different colors refer to different \mathbf{k} points. All the Green's functions decay to 0. Model parameters are $\theta = 1.15^\circ$, $\phi_s = 130^\circ$, $u_0 = 80$ meV and $\epsilon_t = 10$.

problem by construction. As discussed in Methods, by using a Gaussian transformation to decouple the interaction term, we show that the partition function takes the form

$$Z = \int dC W_C, \quad (\text{S56})$$

with

$$W_C = e^{-S_B(C)} \text{Tr} \left(\prod_{\tau} e^{\hat{h}(C_{\tau})} \right) \quad (\text{S57})$$

$$S_B(C) = \frac{1}{2} \sum_i (x_i^2 + p_i^2) \quad (\text{S58})$$

$$\hat{h}(C_{\tau}) = i \sum_{\mathbf{Q}} \left(-x_{\tau, \mathbf{Q}, 1} \sqrt{\alpha(\mathbf{Q})} A_{\mathbf{Q}} + i x_{\tau, \mathbf{Q}, 2} \sqrt{\alpha(\mathbf{Q})} B_{\mathbf{Q}} \right) - \Delta \tau H_0. \quad (\text{S59})$$

The composite index $i \equiv (\tau, \mathbf{Q}, n)$ with $n = 1, 2$ runs over the auxiliary fields, and C_{τ} denotes the auxiliary field configuration at a given Euclidean time τ . Since Z is real, $Z = \int dC \text{Re}W(C)$, and observables are given by

$$\langle \hat{O} \rangle = \frac{1}{Z} \int dC \text{Re}(W_C) \left[\frac{W_C}{\text{Re}W_C} O_C \right] \quad \text{with} \quad O_C = \frac{\text{Tr} \left(\prod_{\tau} e^{\hat{h}(C_{\tau})} \hat{O} \right)}{\text{Tr} \left(\prod_{\tau} e^{\hat{h}(C_{\tau})} \right)}. \quad (\text{S60})$$

$\hat{h}(C_{\tau})$ does not necessarily have the symmetries of the original Hamiltonian, but after integration over field configurations they must be restored since the Gaussian decoupling is exact. For example, in our specific case, $\hat{h}(C_{\tau})$ enjoys the same spin- $SU(2)$ and valley- $U(1)$ symmetries as the original Hamiltonian, but the moiré translation symmetry $\hat{T}_{\mathbf{R}}$ is broken. In particular, the operators in $\hat{h}(C_{\tau})$ transform as

$$\hat{T}_{\mathbf{R}}^{-1} A_{\mathbf{Q}} \hat{T}_{\mathbf{R}} = \cos(\mathbf{Q} \cdot \mathbf{R}) A_{\mathbf{Q}} + i \sin(\mathbf{Q} \cdot \mathbf{R}) B_{\mathbf{Q}} \quad (\text{S61})$$

$$\hat{T}_{\mathbf{R}}^{-1} B_{\mathbf{Q}} \hat{T}_{\mathbf{R}} = \cos(\mathbf{Q} \cdot \mathbf{R}) B_{\mathbf{Q}} + i \sin(\mathbf{Q} \cdot \mathbf{R}) A_{\mathbf{Q}}. \quad (\text{S62})$$

However, translation symmetry will be restored after summation over the field. To see this explicitly from Eq. S60, recall that the presence of a symmetry \hat{U} (i.e. satisfying $[\hat{U}, \hat{H}] = 0$) implies that expectation values satisfy $\langle \hat{U} \hat{O} \hat{U}^{\dagger} \rangle = \langle \hat{O} \rangle$. Taking $\hat{O} \rightarrow \hat{U} \hat{O} \hat{U}^{\dagger}$ in O_C in Eq. S60 induces an effective orthogonal transformation in the auxiliary fields in $\hat{h}(C_{\tau})$ of the numerator according to

$$x_{\tau, \mathbf{Q}, 1} \rightarrow \cos(\mathbf{Q} \cdot \mathbf{R}) x_{\tau, \mathbf{Q}, 1} + \sin(\mathbf{Q} \cdot \mathbf{R}) x_{\tau, \mathbf{Q}, 2} \quad (\text{S63})$$

$$x_{\tau, \mathbf{Q}, 2} \rightarrow \cos(\mathbf{Q} \cdot \mathbf{R}) x_{\tau, \mathbf{Q}, 2} - \sin(\mathbf{Q} \cdot \mathbf{R}) x_{\tau, \mathbf{Q}, 1}. \quad (\text{S64})$$

Denote this transformation as \underline{T} , i.e. $C \rightarrow \underline{T}C$. Owing to the cyclicity of the trace, we have that the denominator of O_C is invariant under $C \rightarrow \underline{T}C$, from which we conclude that $O_C \rightarrow O_{\underline{T}C}$ when considering the expectation value of $\hat{U} \hat{O} \hat{U}^{\dagger}$. Since $S_B(C)$ is invariant under orthogonal transformations, we also find that $W_C = W_{\underline{T}C}$ by cyclicity of the trace. We can therefore

shift integration variables $C \rightarrow T^{-1}C$ (with unit Jacobian) in the expression for $\langle \hat{U} \hat{O} \hat{U}^\dagger \rangle$, demonstrating that $\langle \hat{U} \hat{O} \hat{U}^\dagger \rangle = \langle \hat{O} \rangle$. We can perform a similar analysis for C_2 which transforms $A_{\mathbf{Q}} \rightarrow A_{\mathbf{Q}}$ and $B_{\mathbf{Q}} \rightarrow -B_{\mathbf{Q}}$, and time reversal \mathcal{T} , to show that they are symmetries captured by the measurement of $\langle \hat{O} \rangle$ (despite not being symmetries of $\hat{h}(C_\tau)$).

The sign problem arises from the fact that $\text{Re}W_C$ can be negative for some fields. While it is possible to cope with the sign problem if it is not too severe, one can ask the question whether sampling the partition function

$$\bar{Z} = \int dC |\text{Re}W_C|, \quad (\text{S65})$$

which by construction does not have a sign problem, corresponds to a Hamiltonian \bar{H} with the same symmetries as the original one. The symmetry properties of \bar{H} depend strongly upon the choice of the Hubbard-Stratonovich transformation. For our example, \bar{H} continues to obey all the symmetries because taking $\text{Re}W_C \rightarrow |\text{Re}W_C|$ does not interfere with the property $W_C = W_{TC}$ used above.

In Fig. S5 and S6, we compare the occupation number $n^\tau(\mathbf{k})$ and IVC structure factors between non-approximated QMC (top row), approximated QMC (middle row), and ED (bottom row), for $L = 2, 3$ respectively. As expected, the non-approximated QMC (with the exponential sign problem) and ED calculations agree with each other. We also find qualitative agreement for $n^\tau(\mathbf{k})$ and $S_{\text{KIVC}}(\mathbf{q})$ between approximated QMC and the other exact methods, though the agree for $S_{\text{IKS}}(\mathbf{q})$ is less good.

We now examine whether \bar{H} is a Hermitian operator, which would imply that the density matrix $\bar{\rho} = e^{-\beta \bar{H}}$ is a positive semi-definite Hermitian operator. In the *high* temperature limit where the sign problem is not severe, we expect $\bar{\rho}$ to be proximate to $\hat{\rho}$. At low temperatures, the notion of proximate can be tested explicitly on case-by-case basis by e.g. comparison to exact diagonalization.

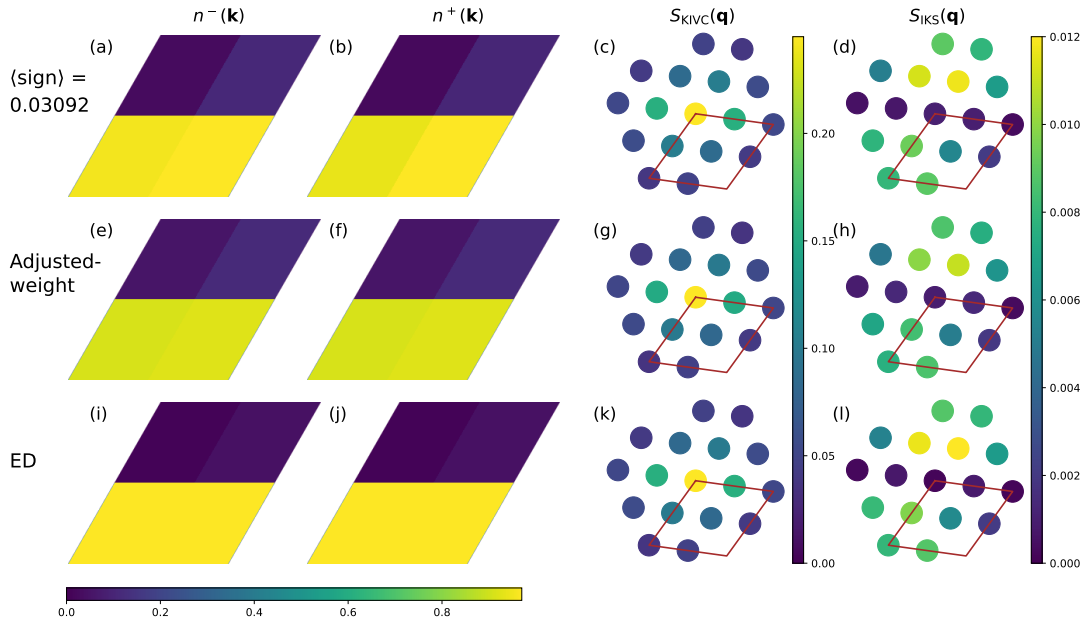


Fig. S5. **Comparison of $n^\tau(\mathbf{k})$ and structure factors from stringent QMC, approximated QMC, and ED with $\epsilon_s = 0.6\%$ and $L = 2$.** We consider the spinless Hamiltonian in these calculations. Note that the parameters are $\theta = 1.15^\circ$, $\phi_s = 130^\circ$, $\epsilon_\tau = 10$, $u_0 = 80$ meV.

The auxiliary field QMC method can be viewed as a sampling of the density matrix $\hat{\rho}$ in the space of Gaussian operators. In particular, we can follow Ref. [56] to write

$$\hat{\rho} = \frac{\int dCW(C) \hat{\rho}(C)}{\int dCW(C)} \quad (\text{S66})$$

with

$$\hat{\rho}(C) = \det G(C) e^{-\hat{c}^\dagger \ln(G^{-1}(C)-1)^{-1} \hat{c}} \quad (\text{S67})$$

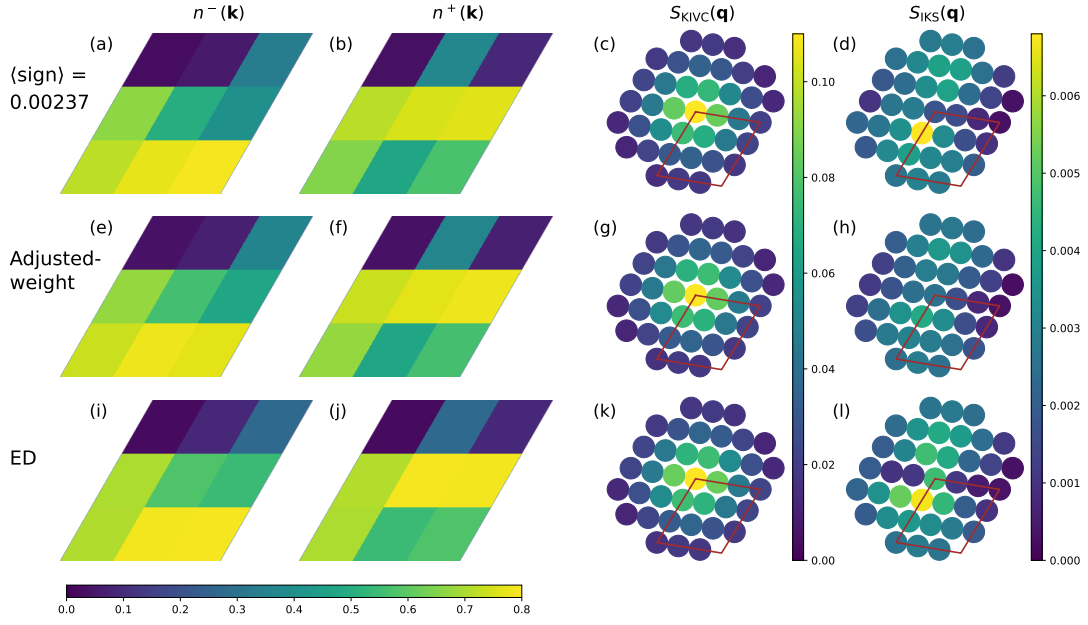


Fig. S6. **Comparison of $n^\eta(\mathbf{k})$ and structure factors from stringent QMC, approximated QMC, and ED with $\epsilon_s = 0.6\%$ and $L = 3$.** We consider the spinless Hamiltonian in these calculations. Note that the parameters are $\theta = 1.15^\circ$, $\phi_s = 130^\circ$, $\epsilon_r = 10$, $u_0 = 80$ meV.

and

$$G(C)_{x,y} = \frac{\text{Tr} \left(\prod_\tau e^{\hat{h}(C_\tau)} \hat{c}_x \hat{c}_y^\dagger \right)}{\text{Tr} \left(\prod_\tau e^{\hat{h}(C_\tau)} \right)}. \quad (\text{S68})$$

Since the density matrix is Hermitian, we can again sample:

$$\hat{\rho} = \frac{\int dC \text{Re}W(C) \frac{1}{2\text{Re}W(C)} (W(C)\hat{\rho}(C) + W^*(C)\hat{\rho}^\dagger(C))}{\int dC \text{Re}W(C)}. \quad (\text{S69})$$

The density matrix associated to $\overline{\hat{H}}$ will then be given by:

$$\overline{\hat{\rho}} = \frac{\int dC |\text{Re}W(C)| \frac{1}{2\text{Re}W(C)} (W(C)\hat{\rho}(C) + W^*(C)\hat{\rho}^\dagger(C))}{\int dC |\text{Re}W(C)|}. \quad (\text{S70})$$

$\overline{\hat{\rho}}$ is thus Hermitian by construction but not necessarily positive such that $\overline{\hat{H}}$ could be non-Hermitian with complex eigenvalues. The imaginary part of the eigenvalue is however quantized to $m\pi/\beta$ due to the Hermiticity of $\overline{\hat{\rho}}$. The particular values of m depend on the model and the applied HS decomposition. We defer a more detailed study of these matters in an upcoming paper. For now, we comment that test calculations on small clusters suggest that the weight of negative eigenvalues of the density matrix tends to be stable in the low- T limit, and disappear in the high- T limit, where the sign problem gradually goes away.

One way to check the presence of non-Hermiticity of the effective Hamiltonian is to look for oscillatory behavior of the Euclidean time-displaced correlators. If a complex eigenvalue λ_C arises, then Euclidean time displaced correlation functions will have a damped oscillatory behavior with period $2\pi/\text{Im}(\lambda_C)$. We have attempted to detect such oscillatory behavior in the single-particle Green's function, the KIVC structure factor and the IKS structure factor, as shown in Fig. S7, Fig. S8 and Fig. S9. However, since $\text{Im}(\lambda_C) = m\pi/\beta$ the period is $2\beta/m$, and would be hard to detect for small values of m . There is also a possibility of our probes being orthogonal to the negative eigenvector of the effective density matrix $\overline{\hat{\rho}}$. Hence we can only conclude that non-Hermiticity of the effective Hamiltonian $\overline{\hat{H}}$ does not obviously manifest itself in single-particle or KIVC (IKS) correlation functions.

Despite the rather different mathematical formulation, we propose that our approximated QMC shares similarities in physical meaning to the dominant thimble approximation in Ref. [57]. In the latter approximation, we neglect the fluctuations of the sign of W_C , because the Monte Carlo field configurations are on a thimble (which is by definition a manifold with fixed sign factor), and

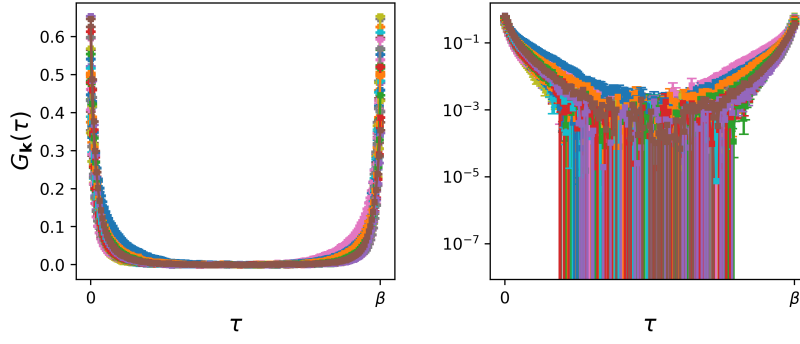


Fig. S7. **Green's functions at $\epsilon_s = 0.6\%$ for $L = 6$ in approximated QMC.** Different colors refer to different \mathbf{k} points. All the Green functions are gapped. Model parameters are $\theta = 1.15^\circ$, $\phi_s = 130^\circ$, $u_0 = 80$ meV and $\epsilon_r = 10$.

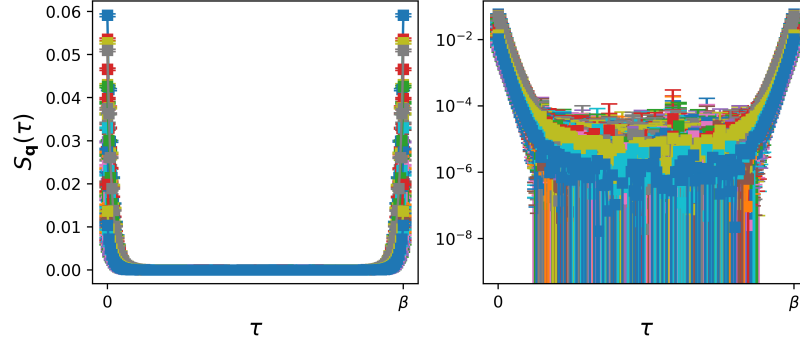


Fig. S8. **KIVC structure factor at $\epsilon_s = 0.6\%$ for $L = 6$ in approximated QMC.** Different colors refer to different \mathbf{q} points. Model parameters are $\theta = 1.15^\circ$, $\phi_s = 130^\circ$, $u_0 = 80$ meV and $\epsilon_r = 10$.

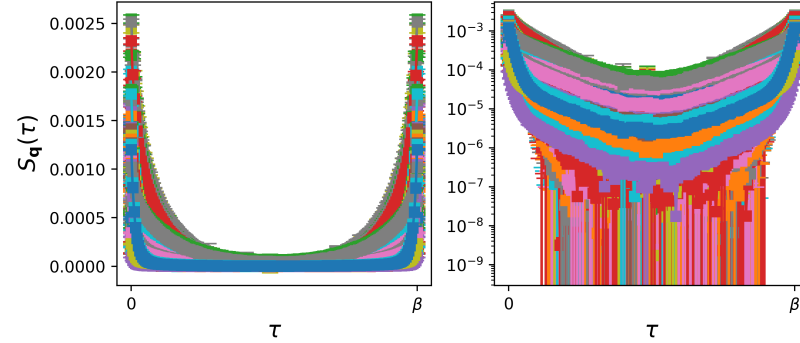


Fig. S9. **IKS structure factor at $\epsilon_s = 0.6\%$ for $L = 6$ in approximated QMC.** Different colors refer to different \mathbf{q} points. Model parameters are $\theta = 1.15^\circ$, $\phi_s = 130^\circ$, $u_0 = 80$ meV and $\epsilon_r = 10$.

we choose the thimble with the maximal weight in the full sum over thimbles forming a partition function. Physically, it means that the saddle point for this thimble captures the correct mean-field solution, and the surrounding thimble gives the fluctuations around it, which can be described neglecting the fluctuations of the sign due to aforementioned mathematical definition of a thimble. Thus, in the approximated QMC, if we are sufficiently close to the mean field solution, similar to the dominant thimble approximation, the fluctuation of the sign might play a lesser role in the description of the fluctuations around this mean field Slater determinant state. We re-iterate though the approximated QMC, and, however, it does not yield long-range IKS order for the parameters we have considered.